

Critical fates induced by the interaction competition in three-dimensional tilted Dirac semimetals

Jing Wang,^{1,2,*} Jie-Qiong Li,¹ Wen-Hao Bian,¹ Qiao-Chu Zhang,¹ and Xiao-Yue Ren¹

¹*Department of Physics, Tianjin University, Tianjin 300072, P.R. China*

²*Tianjin Key Laboratory of Low Dimensional Materials Physics and Preparing Technology, Tianjin University, Tianjin 300072, P.R. China*

(Dated: December 13, 2023)

The interplay among Coulomb interaction, electron-phonon coupling, and phonon-phonon coupling has a significant impact on the low-energy behavior of three-dimensional type-I tilted Dirac semimetals. To investigate this phenomenon, we construct an effective theory, calculate one-loop corrections arising from all these interactions, and establish the coupled energy-dependent flows of all associated interaction parameters by adopting the renormalization group approach. Deciphering such coupled evolutions allows us to determine a series of low-energy critical properties for these materials. At first, we present the low-energy tendencies of all interaction parameters. The tilting parameter exhibits distinct tendencies that depend heavily upon the initial anisotropy of fermion velocities. In comparison, the latter is mainly dominated by its initial value but is less sensitive to the former. Variations in these two quantities drive certain interaction parameters toward the strong anisotropy in the low energy regime, indicating the screened interaction in specific directions, and others toward an approximate isotropy. Additionally, we observe that the tendencies of interaction parameters can be qualitatively clustered into three distinct types of fixed points, accompanied by the potential instabilities that induce certain interaction-driven phase transition. Furthermore, approaching these fixed points leads to the critical behavior of physical quantities, such as the density of states, compressibility, and specific heat, which exhibit quite different from their non-interacting counterparts and even deviate slightly from Fermi-liquid behavior. Our investigation sheds light on the intricate relationship between different types of interactions in these semimetals and provides useful insights into their fundamental properties.

I. INTRODUCTION

In recent years, the study of Dirac semimetals (DSM), featuring the intermediate properties between metals and insulators, has become one of the most active fields in contemporary condensed matter physics [1–19]. Typically, DSMs possess the Dirac cones and reduced Fermi surfaces composed of discrete Dirac points, exhibiting gapless low-energy excitations irrespective of the microscopic details. These materials display linear energy dispersions along two or three directions [1–3, 10, 11, 11–13, 16–24]. In particular, their unique properties are guaranteed and protected by kinds of symmetries, including time-reversal, space-reversal symmetry, etc. [2, 14]. However, these Dirac cones can be stretched and thus tilted by breaking a certain fundamental symmetry (such as t -Lorentz symmetry) [25–27] or via an additional force in a certain direction [28]. Consequently, the energy dispersions become anisotropic, resulting in unequal fermion velocities along distinct directions. Henceforth, these materials are known as the tilted Dirac semimetals (tDSM) [25, 25–33, 33]. Besides two-dimensional (2D) tilted Dirac cones were reported in an organic compound $\alpha - (\text{BEDT} - \text{TTF})_2\text{I}_3$ and certain mechanically deformed graphene [34–36], three-dimensional (3D) tilted cones have also been realized later in WTe_2 [25]

and the Fulde-Ferrell ground state of a spin-orbit coupled fermionic superfluid [37] or a cold-atom optical lattice [38]. Conventionally, the tDSM can be categorized into two distinct types based on the tilted angles. Type-I tDSM retains analogous Dirac cones as long as the tilted angle is insufficient to destroy the point-like Fermi surface [33, 39]. In contrast, for Type-II tDSM, such as PdTe_2 [31, 32] and PtTe_2 [40], the Dirac point would be replaced by two straight lines, indicating the open Fermi surface once the tilted angle reaches a sufficient magnitude [25, 27, 29].

These tilted materials have recently garnered significant attention owing to their unique low-energy excitations and tilted Dirac cones [26, 29, 30, 41–56]. Particularly, the effects of Coulomb interaction and impurities on the low-energy properties of tDSM were investigated by many groups [29, 30, 41, 49]. However, previous studies on 3D tDSM have insufficiently considered several physical ingredients, such as phonons and electron-phonon interactions, and their interplay with Coulomb interaction. These additional degrees of freedom may play a critical role in determining the low-energy behavior of 3D tDSM. Neglecting them could result in the partial or incomplete capture of important physical information that is closely associated with such interactions. Therefore, to enhance our understanding of 3D tilted materials, it is essential to carefully examine how the interplay between Coulomb interaction and electron-phonon coupling affects the low-energy behavior of 3D tDSMs.

Without loss of generality, we within this work con-

*Corresponding author: jing_wang@tju.edu.cn

centrate on the type-I 3D tDSM. Compared to their 2D counterparts, these materials are more complicated but interesting. On one hand, as the density of the state of fermionic quasiparticles vanishes as approaching the Dirac point of type-I tDSM [33, 39, 49], it is necessary to take into account the effects of long-range Coulomb interaction between low-energy fermionic excitations, which is marginal at the tree level in the RG language. On the other hand, the lattice vibrations in 3D materials are more intricate and lead to the emergence of (acoustic or optical) phonons. These phonons exhibit different internal properties for ionic and covalent crystals (For the sake of simplicity, this work is restricted to the latter, wherein the coupling between phonon and Coulomb auxiliary field vanishes) [57]. Phonons not only interact with each other via phonon-phonon interactions but also inevitably entangle with low-energy fermions, potentially competing indirectly with Coulomb interaction. In this context, we expect phonons and their related consequences to play an essential role in governing the low-energy physics of 3D tDSM. To investigate the unusual behavior of 3D tDSM in the low-energy regime, we are therefore forced to take into account all these items on the same footing.

To this end, we employ the powerful renormalization group (RG) approach [58–60] to treat all physical ingredients mentioned above on the same footing. Specifically, we construct the effective theory for type-I tDSM and derive the coupled energy-dependent evolutions of all interaction parameters by carrying out the energy-shell RG analysis. Subsequently, after performing a numerical analysis of such evolutions, we systematically investigate the low-energy fates of these interactions and elucidate their implications on the 3D tDSM.

At first, we examine the behavior of various interaction parameters in the low-energy regime, considering the intimate competition among them. To be specific, we find that the tilting parameter is insensitive to its initial value but is significantly influenced by the starting anisotropy of fermion velocities. Regarding the fermion velocities, their ratio can either increase, decrease, or remain nearly unchanged in the low-energy regime, depending upon their initial anisotropy and tilting parameter. Turning attention to the dielectric constant, which characterizes the strength of Coulomb interaction, we notice its tendency to exhibit a strong anisotropy in the low-energy regime, indicating the screened Coulomb interaction in a certain direction. In comparison, both phonon velocities and phonon-phonon interaction can either flow towards the approximate isotropy or exhibit the basic results of the dielectric constant by flowing towards an extreme anisotropy in the low-energy regime. It is of also noteworthy to point out that the coupling strength of electron-auxiliary bosonic interaction and the electron-phonon interactions bear similar behavior to that of the dielectric constant and phonon velocities, respectively.

In addition, we identify three kinds of fixed points by categorizing the energy-dependent tendencies of all interaction parameters and then investigate the leading insta-

stabilities around such fixed points. Furthermore, the critical tendencies of physical quantities, including the density of states and compressibility as well as specific heat, are carefully studied as the system approaches these three distinct types of fixed points. They present different but interesting behavior compared to their non-interacting counterparts.

The rest of this work is organized as follows. In Sec. II we present the microscopic model and outline the low-energy effective theory. The Sec. III is followed to bring out the RG transformations and then derive the coupled energy-dependent RG equations of all interaction parameters in our effective theory after taking into account all one-loop corrections. Afterwards, we within Sec. IV delve into the tendencies and fates of these interaction parameters in the low-energy regime by examining evolved the RG flows. Moving forward to Sec. V and Sec. VI, we present the dominant instabilities and behavior of physical implications as the system approaches the fixed points, respectively. Finally, a brief summary is provided in Sec. VII.

II. MICROSCOPIC MODEL AND EFFECTIVE THEORY

We focus our attention on the 3D tDSM, characterized by an additional term that tilts the energy bands. Armed with the microscopic structure of 3D tDSM, the non-interacting Hamiltonian density in the low-energy regime can be formally expressed as follows [29, 36, 49]

$$\mathcal{H}_0 = \zeta v_z k_z \sigma_0 + \chi [v_z k_z \sigma_z + v(k_x \sigma_x + k_y \sigma_y)], \quad (1)$$

where v and v_z denote the fermion velocities along the oxy plane and z direction perpendicular to such plane, respectively. In addition, $\chi = \pm 1$ stands for the chirality symmetry of Dirac point, as well as σ_i with $i = 1, 2, 3$ corresponds to the Pauli matrices, while σ_0 represents the identity matrix.

Hereby, the dimensionless parameter ζ in Eq. (1) serves as a tilting parameter that enters into the energy dispersions as follows

$$E_{\pm}(\mathbf{k}) = \zeta v_z k_z \pm \sqrt{(v_z k_z)^2 + (v k_x)^2 + (v k_y)^2}. \quad (2)$$

As a consequence, the presence of this very parameter can modify and reshape the overall structure of the Fermi surface by tilting the Dirac cones [29, 36, 49]. In practice, this necessitates the categorization of two distinct types of the tDSM [29]. The first type, termed type-I tDSM, occurs when $|\zeta| < 1$. As to the type-I tDSM, the point-like Fermi surface remains robust, and the renormalized Dirac cones are preserved against tilted contributions. Instead, the other type dubbed the type-II tDSM, emerges when the tilted term plays a more significant role in shaping the Fermi surface at $|\zeta| > 1$. In this case, the point-like structure of the Fermi surface is sabotaged and replaced by two crossed nodal lines [29, 30].

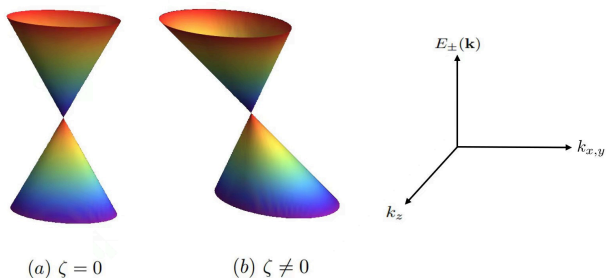


FIG. 1: (Color online) Schematic dispersion for (a) the un-tilted and (b) the tilted 3D DSM, respectively.

To proceed, we hereafter restrict our study to the 3D type-I tDSM, namely $|\zeta| < 1$ in Eq. (2) as schematically illustrated in Fig. 1. Starting from the Hamiltonian density in Eq. (1), we are left with the following noninteracting fermionic action,

$$S_{\psi} = \sum_{\chi, \alpha} \int_{\mathbf{k}} \psi_{\chi\alpha}^{\dagger}(\omega, \mathbf{k}) \{i\omega\sigma_0 - \zeta v_z k_z \sigma_0 - \chi [v_z k_z \sigma_z + v(k_x \sigma_x + k_y \sigma_y)]\} \psi_{\chi\alpha}(\omega, \mathbf{k}), \quad (3)$$

with $\int_{\mathbf{k}} = \int d\omega d^3\mathbf{k}/(2\pi)^4$. Here, the spinors $\psi_{\chi\alpha}^{\dagger}(\omega, \mathbf{k})$ and $\psi_{\chi\alpha}(\omega, \mathbf{k})$ with spin degeneracy $\alpha = \pm 1$ describe the excited fermionic quasiparticles from the Dirac points in the first Brillouin zone [29, 36, 49]. As we only consider the type-I tDSM, the tilting parameter is constrained to $|\zeta| \in (0, 1)$ with $\zeta \rightarrow 0$ corresponding to the normal (un-tilted) 3D Dirac systems. It is worth highlighting that the tilted energy dispersion (2) indicates that the tilted Dirac cones are symmetric under the sign change of the tilting parameter. Without loss of generality, we from now on restrict our study to the situation with a positive ζ . In addition, one can expect that the velocities are no longer isotropic but become anisotropic for the tilted direction (v_z) and the other two orientations (v) in the presence of the tilted terms. To proceed, the free fermionic propagator can be readily derived from Eq. (3).

$$G_0^{-1}(k) = (i\omega - \zeta v_z k_z) \sigma_0 - \chi [v_z k_z \sigma_z + v(k_x \sigma_x + k_y \sigma_y)]. \quad (4)$$

In addition to the fermionic excitations (1), we incorporate the contributions from phonons, which signify the potential lattice distortions. Since the optical phonons are much more important than acoustic ones as approaching the potential instability in the low-energy regime, we here only focus on the former [57]. In principle, there exist two different kinds of modes corresponding to the transverse phonon and longitudinal phonon. Accordingly, the relevant phonon ingredients can be expressed as [57, 61, 62]

$$S_u = \int d^4x \frac{1}{2} u_j(x) [(-\partial_0^2) \delta_{ji} - C_T^2 (\nabla^2 \delta_{ji} - \partial_j \partial_i) - C_L^2 \partial_j \partial_i] u_i(x) + V \int d^4x [u_j(x) u_j(x)]^2, \quad (5)$$

where u_i (u_j) represents the phonon field with $i, j = x, y, z$, and $C_{T,L}$ specify the velocities of the transverse and longitudinal phonons, while the coupling V characterizes the self-interactions among phonons themselves. In principle, the transverse phonon owns an “effective mass” that can be utilized as a tuning parameter. For simplicity, we hereby assume it to be small enough and neglect, given that the concerned regime is adjacent to the potential phase transition where the phonons become gapless [57]. Under this assumption, the free transverse and longitudinal phonon propagators in the momentum space can be written as,

$$G_{u,ji}^T(q_0, \mathbf{q}) = \frac{\delta_{ji} - \hat{q}_j \hat{q}_i}{q_0^2 - \omega_T^2 + C_T^2}, \quad (6)$$

$$G_{u,ji}^L(q_0, \mathbf{q}) = \frac{\hat{q}_j \hat{q}_i}{q_0^2 + C_L^2 \mathbf{q}^2}, \quad (7)$$

with $\hat{q}_j \hat{q}_i \equiv q_j q_i / \mathbf{q}^2$ for $i, j = x, y, z$. Besides their self-interactions in Eq. (5), the phonons are expected to couple with the fermionic excitations, and this coupling can be constructed as follows [57],

$$S_{u\psi} = \sum_j \lambda_j \int d^4x \psi^{\dagger} \sigma_j \psi u_j, \quad (8)$$

where the coupling λ_j with $j = x, y, z$ are utilized to measure the strength between fermions and phonons.

Furthermore, it is of particular significance to take into account the Coulomb interaction among the low-energy fermionic excitations. For the sake of simplicity, such degrees of freedom can be effectively established by introducing an auxiliary bosonic field ϕ as [24, 29, 57, 63–65]

$$S_{\text{Coul}} = \frac{1}{2} \int_{\mathbf{q}} \phi(q_0, \mathbf{q}) D_0^{-1}(\mathbf{q}) \phi(-q_0, -\mathbf{q}) + ig \int_{\mathbf{q}} \phi(q_0, \mathbf{q}) \psi^{\dagger}(\omega + q_0, \mathbf{k} + \mathbf{q}) \sigma_0 \psi(\omega, \mathbf{k}), \quad (9)$$

where the free propagator for auxiliary bosonic field is given by

$$D_0(\mathbf{q}) = \frac{4\pi}{\epsilon \mathbf{q}^2}. \quad (10)$$

Here, the parameter ϵ serves as the dielectric constant, and g characterizes the coupling strength between fermion and the auxiliary bosonic field.

Based on above presentations, we gather the physical elements, including the low-energy fermionic excitations (3) and phonons (5), in conjunction with their entanglements (8)-(9), and eventually arrive at our effective theory,

$$S_{\text{eff}} = S_{\psi} + S_u + S_{u\psi} + S_{\text{Coul}}, \quad (11)$$

where the corresponding free propagators for fermion, phonon, and the auxiliary bosonic field are presented in

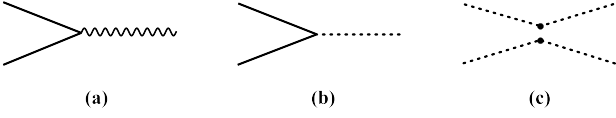


FIG. 2: Tree-level vertices: (a) Coulomb interaction, (b) electron-phonon interaction, and (c) phonon-phonon interaction, respectively (the solid, wavy, and dashed lines denote the free fermionic, auxiliary bosonic, and phonon propagators).

Eq. (4), Eqs. (6)-(7), and Eq. (10), respectively. Additionally, the associated tree-level vertices for the interactions among low-energy fermion and phonons are illustrated in Fig. 2. With these in hand, it is suitable to construct all the one-loop diagrams contributing to the interaction parameters, as detailed in Appendix A. Subsequently, we adopt the effective action (11) as our starting point to examine the critical fates of 3D tDSM in the low-energy regime, taking into account the influence of Coulomb interaction, electron-phonon interaction, and phonon-phonon interaction.

III. RG ANALYSIS AND COUPLED EVOLUTIONS

Given the distinctive energy dispersions characterized by the tilted Dirac cones in type-I 3D tDSM, it is appropriate to adopt the energy-shell method for the RG analysis [58–60]. This henceforth requires us to integrate the energy shells out one by one during the RG transformations [29, 42, 60, 66–68]. To this end, we introduce the useful transformations and then utilize the Jacobian transformation to parameterize the tilted energy dispersion (2). This parameterization is expressed as follows [29, 30, 36, 42]

$$v_z k_z = -\frac{\zeta}{1-\zeta^2}E + \frac{|E|}{1-\zeta^2} \cos \theta, \quad (12)$$

$$v k_x = \frac{|E|}{\sqrt{1-\zeta^2}} \sin \theta \cos \varphi, \quad (13)$$

$$v k_y = \frac{|E|}{\sqrt{1-\zeta^2}} \sin \theta \sin \varphi, \quad (14)$$

$$\int dk_x dk_y dk_z = \int dE \int_0^\pi d\theta \int_0^{2\pi} d\varphi \frac{E^2 \sin \theta (\eta_E - \zeta \cos \theta)}{v^2 v_z (1-\zeta^2)^2}, \quad (15)$$

where E denotes the energy scale with the η_E collecting its sign, as well as θ and φ are two associated angles. In the spirit of the energy-shell framework, the fast modes of degrees of freedom within the energy shell $\Lambda/b < E < \Lambda$ would be integrated out, where Λ is the energy scale and variable parameter b can be specified as $b = e^{-l} < 1$ with $l > 0$. Then, the renormalized “slow modes” are obtained, with which the RG processes can be fulfilled by performing the RG transformation rescalings [58–60].

To proceed, we are going to derive the RG rescaling transformations that serve as crucial bridges connecting

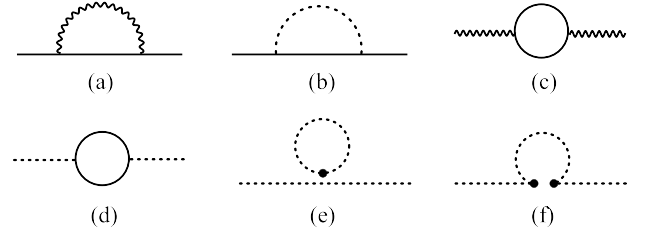


FIG. 3: One-loop corrections caused by the Coulomb and electron-phonon as well as phonon-phonon interactions to (a)-(b) fermionic propagator, (c) auxiliary bosonic propagator, and (d)-(f) phonon propagator, respectively (the solid, wavy, and dashed lines denote the free fermionic, auxiliary bosonic, and phonon propagators).

two successive RG steps. Following the RG approach [58–60], the free frequency term in the non-interacting action (3) can be regarded as the initial fixed point that is invariant during the RG process. In the collaborations with Eqs. (12)-(15), it accordingly gives rise to the following RG rescalings [29, 30, 60, 66–68],

$$\omega \longrightarrow \omega' e^{-l}, \quad (16)$$

$$E \longrightarrow E' e^{-l}, \quad (17)$$

$$\psi \longrightarrow \psi' e^{\frac{5}{2}l - \eta_\psi l}, \quad (18)$$

$$\phi \longrightarrow \phi' e^{3l - \eta_\phi l}, \quad (19)$$

$$u_T \longrightarrow u'_T e^{3l - \eta_{u_T} l}, \quad (20)$$

$$u_L \longrightarrow u'_L e^{3l - \eta_{u_L} l}, \quad (21)$$

where η_ψ , η_ϕ , η_{u_T} , and η_{u_L} are the anomalous dimensions of related fields that capture the one-loop corrections due to all kinds of interactions in our effective theory (11). To determine them, we resort to the one-loop contributions to the free propagators as shown in Fig. 3. The straightforward calculations gives rise to

$$\Sigma_f(i\omega, \mathbf{k}) = -\{[i\omega \mathcal{A}_0 - \zeta v_z k_z \mathcal{A}_3] \sigma_0 - \chi [\mathcal{A}_2 v_z k_z \sigma_z + v \mathcal{A}_1 (k_x \sigma_x + k_y \sigma_y)]\} l, \quad (22)$$

$$\Sigma_b(\mathbf{q}) = \frac{-[v^2 (q_x^2 + q_y^2) + v_z^2 q_z^2] g^2 l}{4\pi^2 v^2 v_z (1-\zeta^2)}, \quad (23)$$

$$\Sigma_{u_{T,L}}(q_0) = \frac{-5\lambda_j \lambda_i \delta_{ji} q_0^2 l}{2\pi^2 v^2 v_z}, \quad (24)$$

for fermionic, auxiliary bosonic, and phonon propagators, respectively. Here, the coefficients $\mathcal{A}_{0,1,2}$ are designated in Eqs. (A5), (A6), and (A11) of Appendix A. Consequently, such one-loop corrections lead to [66–68]

$$\eta_\psi = -\frac{\mathcal{A}_0}{2}, \quad \eta_\phi = 0, \quad \eta_{u_L^j} = \eta_{u_T^j} = -\frac{5\lambda_j^2}{8\pi^2 v^2 v_z}, \quad (25)$$

with $j = x, y, z$ as aforementioned in Eq. (8). Subsequently, the detailed calculations of one-loop corrections to the interaction vertices are presented in Appendix A. After combining the RG rescaling transformations (16)-(21) with the anomalous dimensions (25) and all one-

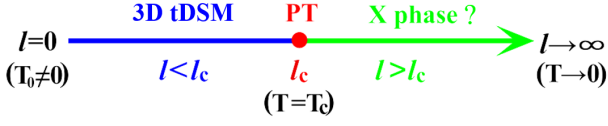


FIG. 4: (Color online) A schematic diagram illustrating the tendencies of 3D tDSM and potential instability as the energy scale is tuned. The label l_c (or T_c) specifies the critical energy scale (or critical temperature) and “PT” designates the accompanying phase transition induced by the potential instability from the 3D tDSM to an X phase. A further investigation into this transition will be conducted in Sec. V.

loop corrections in Appendix A, the coupled RG equations of all interaction parameters are derived as follows [29, 60, 66–68]

$$\frac{dv}{dl} = (-\mathcal{A}_1 - 2\eta_\psi)v, \quad (26)$$

$$\frac{dv_z}{dl} = (-\mathcal{A}_2 - 2\eta_\psi)v_z, \quad (27)$$

$$\frac{d\zeta}{dl} = (\mathcal{A}_2 - \mathcal{A}_3)\zeta, \quad (28)$$

$$\frac{d\epsilon}{dl} = \frac{g^2}{\pi v_z(1 - \zeta^2)}\epsilon, \quad (29)$$

$$\frac{d\epsilon_z}{dl} = \frac{v_z g^2}{\pi v^2(1 - \zeta^2)}\epsilon_z, \quad (30)$$

$$\frac{dC_{T,L}}{dl} = -\eta_{u_x} C_{T,L}, \quad (31)$$

$$\frac{dC_{T,L}^z}{dl} = -\eta_{u_z} C_{T,L}^z, \quad (32)$$

$$\frac{dg}{dl} = (\mathcal{B} - 2\eta_\psi)g, \quad (33)$$

$$\frac{d\lambda}{dl} = (\mathcal{D} - 2\eta_\psi - \eta_{u_x})\lambda, \quad (34)$$

$$\frac{d\lambda_z}{dl} = (\mathcal{D}_z - 2\eta_\psi - \eta_{u_z})\lambda_z, \quad (35)$$

$$\frac{dV_{T,L}^{xx}}{dl} = (-4\eta_{u_x} - \mathcal{F}_{T,L}^{xx})V_{T,L}^{xx}, \quad (36)$$

$$\frac{dV_{T,L}^{zz}}{dl} = (-4\eta_{u_z} - \mathcal{F}_{T,L}^{zz})V_{T,L}^{zz}, \quad (37)$$

$$\frac{dV_{T,L}^{xy}}{dl} = [-(2\eta_{u_x} + 2\eta_{u_y}) - \mathcal{F}_{T,L}^{xy}]V_{T,L}^{xy}, \quad (38)$$

$$\frac{dV_{T,L}^{xz}}{dl} = [-(2\eta_{u_x} + 2\eta_{u_z}) - \mathcal{F}_{T,L}^{xz}]V_{T,L}^{xz}. \quad (39)$$

Here, all the associated coefficients $\mathcal{A}_{1,2,3}$, \mathcal{B} , \mathcal{D} , \mathcal{D}_z , and $\mathcal{F}_{T,L}$ are designated in Appendix A. It is worth emphasizing that the directions x and y are isotropic as displayed in Eq. (1). As a consequence, several flows of parameters, including $V^{yy}T, L$ and $V_{T,L}^{yz}$, similar to their xx and xz -component counterparts, can be neglected to simplify our analysis.

The energy-dependent coupled evolutions (26)-(39) encapsulate the low-energy information resulting from the interplay among all interactions in our effective the-

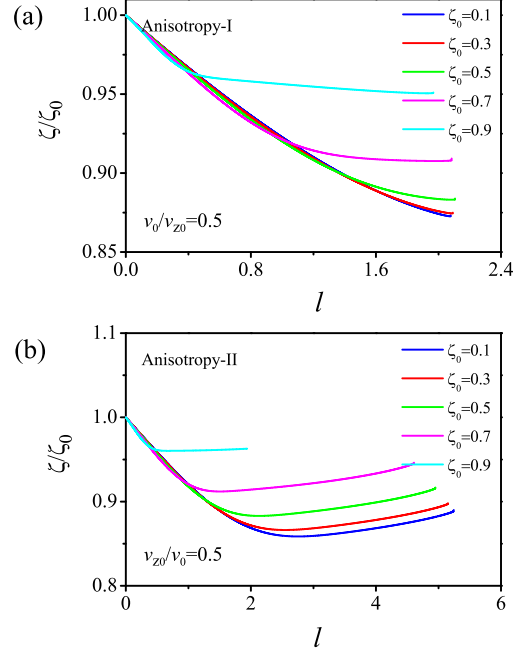


FIG. 5: (Color online) Energy-dependent evolutions of ζ/ζ_0 as ζ_0 varies, starting from (a) Anisotropy-I ($v_0/v_{z0} = 0.5$) and (b) Anisotropy-II ($v_{z0}/v_0 = 0.5$) situations, respectively.

ory. Deciphering the physics encoded in these equations, Fig. 4 schematically presents the underlying properties from the initial state to the lowest energy limit. We realize that the competition among different sorts of interactions results in a number of unique behavior as the energy scale decreases. In particular, it potentially induces some instability, which may drive a phase transition from a 3D tDSM to an X phase as the critical energy scale denoted by l_c is approached. Our primary focus hereafter is on studying these low-energy consequences. Specifically, we are going to investigate the tendencies of interaction parameters and their related implications at $l < l_c$ in the upcoming section IV. The examination of potential instability at $l \rightarrow l_c$ (depicted in Fig. 4) and critical behavior as l approaches l_c will be discussed in Sec. V and Sec. VI, respectively.

IV. TENDENCIES AND FATES OF INTERACTION PARAMETERS

As aforementioned in Sec. III, the coupled RG evolutions encompass all the low-energy properties of 3D tDSM influenced by Coulomb interaction as well as electron-phonon and phonon-phonon interactions. We within this section are going to investigate the energy-dependent coupled RG flow equations and endeavor to extract the low-energy behavior of all relevant parameters from the intimate competition of these interactions.

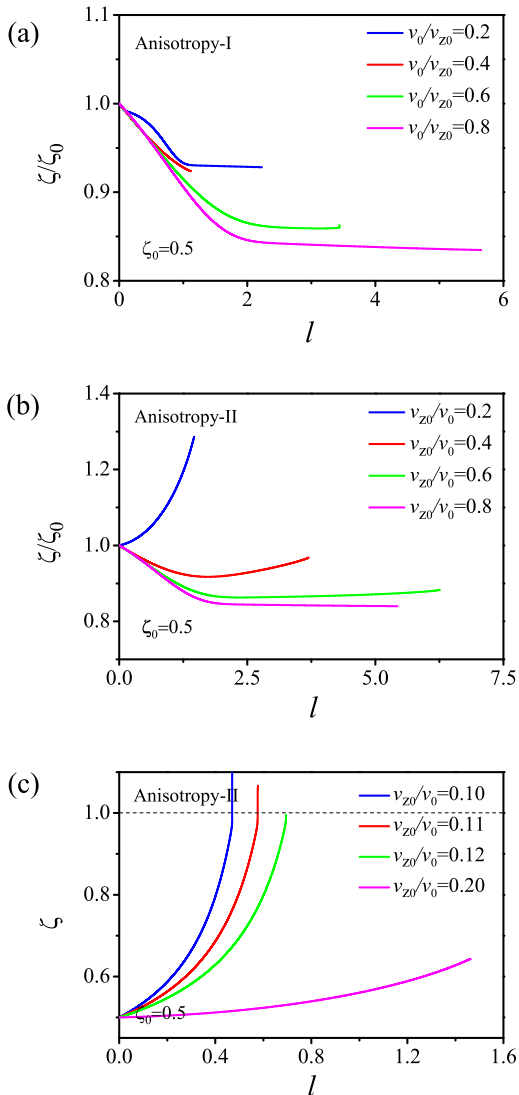


FIG. 6: (Color online) Energy-dependent evolutions of ζ/ζ_0 with variation of v_{z0}/v_0 , starting from (a) Anisotropy-I, (b) Anisotropy-II situations, and (c) of ζ for Anisotropy-II case, respectively.

A. Fate of ζ/ζ_0 and two unstable scenarios

Before proceeding further, it is of particular necessity to highlight the effective theory (11) is restricted to the type-I tDSM with $\zeta \in (0, 1)$. To ensure the well-defined RG equations, we accordingly commence with examining the low-energy behavior of the tilting parameter ζ . For convenience of reference in future discussions, we designate the system with $v_0 < v_{z0}$, $v_0 > v_{z0}$, $v_0 = v_{z0}$ as the Anisotropy-I, Anisotropy-II, and Isotropic cases, respectively.

As discussed in Sec. II, we hereby put our focus on the $\zeta > 0$ case due to the symmetric consideration. Carrying out the numerical analysis of RG equations (26)-(39)

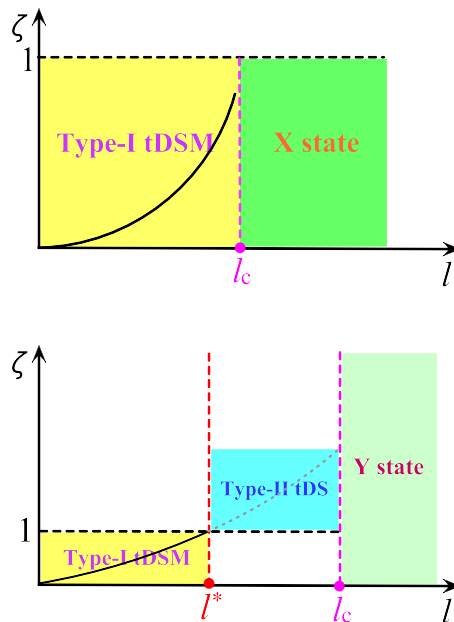


FIG. 7: (Color online) A schematic diagram illustrates two distinct scenarios for the phase transition: (a) transitioning to the X state characterized by $\zeta < 1$, and (b) transitioning to Y state with $\zeta > 1$, respectively.

gives rise to the basic properties of ζ in Figs. 5-6. At first, we fix the initial values of fermion velocities and study the evolution of ζ for several representative initial values. Fig. 5(a) illustrates that in the Anisotropy-I case, ζ/ζ_0 decreases with lowering energy scales, and finally converges to a finite value that is always less than 1 at a certain value. In comparison, Fig. 5(b) showcases ζ/ζ_0 in the Anisotropy-II initially decreases and then increases in the low energy regime, yet remains constrained to $\zeta/\zeta_0 \leq 1$. Interestingly, we notice that the decrease in energy scale has a relatively less pronounced effect on ζ/ζ_0 for a bigger initial tilting system. The Isotropic case exhibits similar basic results. As a consequence, the type-I tDSM is adequately robust against the variations in the initial values of fermion velocities, ensuring the validity of the coupled RG equations.

Next, we study the stability of the tilting parameter under varying values of fermion velocities. Given the observed robustness of ζ to changes in its initial value for both Anisotropy-I and Anisotropy-II scenarios as shown in Fig. 5, it is suitable to select a fixed ζ_0 and examine its behavior by tuning the fermion velocities. Fig. 6(a) signals that, in the Anisotropy-I case, ζ/ζ_0 decreases and gradually reaches a finite value within the type-I tDSM. Considering the Anisotropy-II case, depicted in Fig. 6(b), we observe similarities in the behavior of ζ/ζ_0 to that of Anisotropy-I when $v_z/v_0 < 0.4$. However, at $v_z/v_0 = 0.4$, there is a tendency for ζ/ζ_0 to increase, reaching 1.3 at $v_0/v_{z0} = 0.2$. Even though ζ is still less than 1 with $\zeta/\zeta_0 = 1.3$, this suggests a potential for ζ to exceed 1, indicating a departure from the type-I tDSM. These

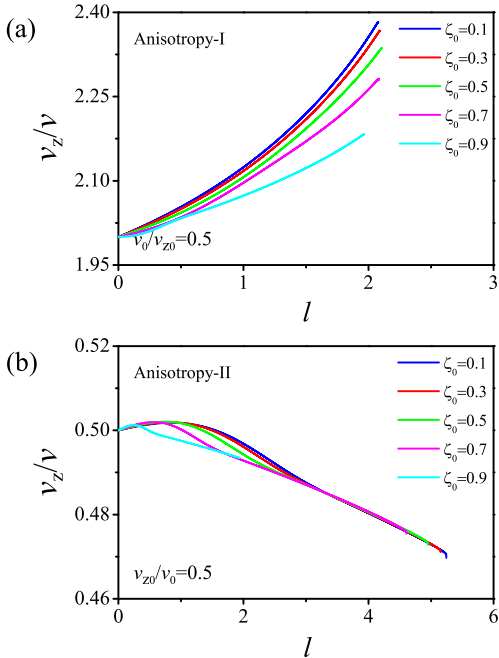


FIG. 8: (Color online) The energy-dependent evolutions of v_z/v are depicted with respect to the variation of ζ_0 , starting from (a) Anisotropy-I and (b) Anisotropy-II situations, respectively.

findings imply the significance of fermion velocities in influencing the stability and nature of ζ .

To verify this, we provide Fig 6(c), which includes more initial values for the Anisotropy-II case. It exhibits that the ζ is indeed capable of exceeding 1 at $v_{z0}/v_0 \approx 0.12$. In particular, the tilting parameter experiences a more rapid increase and gains a bigger value while v_{z0}/v_0 is smaller than 0.12. In this sense, we infer that the critical ratio of fermion velocities initiates the transition from the Type-I tDSM to Type-II tDSM in the vicinity of $v_{z0}/v_0 \approx 0.12$. Schematically depicted in Fig. 7, there exist two possible scenarios for such a transition. In the first scenario, the Type-I tDSM undergoes a direct transition to an X state at l_c as illustrated in Fig. 7(a), driven by the competition among Coulomb interaction and electron-phonon coupling as well as phonon-phonon interaction. In the second scenario, shown in Fig. 7(b), the Type-I tDSM first transitions to Type-II tDSM at $l_* < l_c$ before entering into a Y state.

To recapitulate, the tilting parameter ζ is robust with respect to its initial value, but relatively sensitive to the ratio of fermion velocities. In particular, we identify that a critical value of the ratio, $v_{z0}/v_0 \approx 0.12$, below which the Type-I tDSM becomes unstable and can potentially transition to the Type-II tDSM. However, our effective theory is confined to the Type-I tDSM, and hence the coupled RG equations are only well-defined within this context. Consequently, we from now on will only consider the first scenario as displayed in Fig. 7(a) and investigate the behavior of all other related parameters in

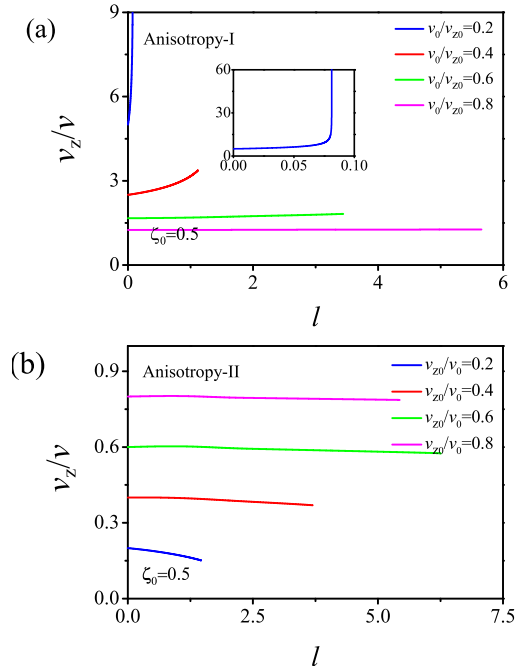


FIG. 9: (Color online) The energy-dependent evolutions of v_z/v are depicted with respect to the variations of initial fermion velocities, starting from (a) Anisotropy-I and (b) Anisotropy-II situations, respectively.

the remainder of this section. Further, we will judge the candidate phase for X state and explore the physical implications in the next two sections.

B. Fates of fermion velocities

In the context of Type-I tDSM, we begin with studying the impacts of interactions on fermion velocities. Fig. 8 illustrates the basic tendencies of the anisotropy of fermion velocities v_z/v . Starting from the Anisotropy-I case, one can read from Fig. 8(a) that as the energy scale decreases, v_z/v progressively increases and the weaker tilting parameter is preferable to support this increase. In sharp contrast, as illustrated in Fig. 8(b), the ratio v_z/v receives a slight increase initially when deviating from the Anisotropy-II, but it subsequently decreases to a certain value as the energy scale diminishes. Besides, both its evolution and the final value of this ratio are fairly insensitive to the tilting parameter, which are distinct from its Anisotropy-I counterpart. This implies that the qualitative behavior of anisotropy of fermion velocities heavily relies on its beginning value in comparison to the strength of the tilting parameter.

It is therefore necessary to further investigate the influence of the initial condition of anisotropy on the low-energy fate of fermion velocities. As shown in Fig. 9 with several initial values of v/v_z , we adopt a representative tilting parameter $\zeta_0 = 0.5$ to show the energy-dependent anisotropy of fermion velocities for both Anisotropy-

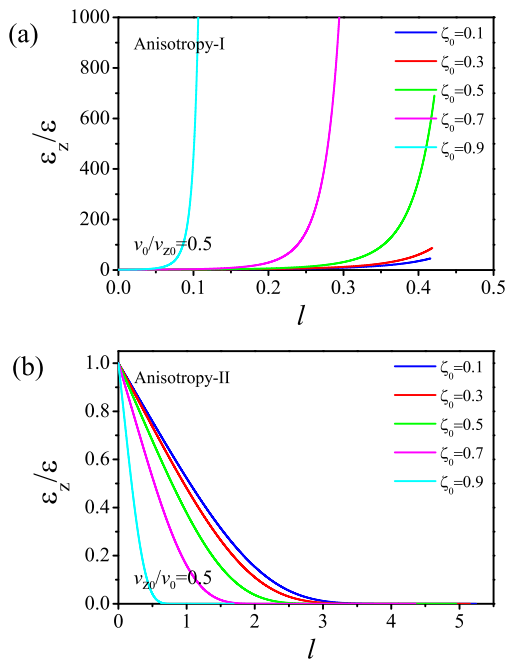


FIG. 10: (Color online) The energy-dependent evolutions of ϵ_z/ϵ are depicted with respect to the variations of ζ_0 , starting from (a) Anisotropy-I and (b) Anisotropy-II situations, respectively.

I and Anisotropy-II. Specifically, for the Anisotropy-I, the anisotropy of fermion velocities v_z/v is primarily dependent on its initial anisotropy. As displayed in Fig. 9(a), v_z/v is insusceptible to the energy scales, remaining relatively stable in the presence of a weak starting anisotropy. However, with a strong initial anisotropy, it becomes sensitive and experiences rapid growth. In contrast, Fig. 9(b) indicates that the v_z/v , departing from Anisotropy-II, can only receive slight negative corrections and even become saturated when the starting anisotropy is adequately weak. Therefore, we infer that the fate of v_z/v predominantly hinges upon the initial anisotropy. In addition, it is sensitive to the value of v_0/v_{z0} and ζ_0 when starting from Anisotropy-I and Anisotropy-II, respectively.

C. Fates of ϵ_z/ϵ and g/g_0

Subsequently, we move to investigate the impacts of coupled interactions on the dielectric constant, which is an important quantity to measure the strength of Coulomb interactions. Given the focus is put on a tilted 3D tDSM, we are more interested in examining the ratio of dielectric constant between different orientations. By selecting a specific initial ratio of fermion velocities, Fig. 10 clearly displays that, in the case of Anisotropy-I ($v_0/v_{z0} = 0.5$), ϵ_z/ϵ quickly increases. Conversely, it decreases rapidly to zero in Anisotropy-II ($v_{z0}/v_0 = 0.5$). Despite these results are robust under the variations of

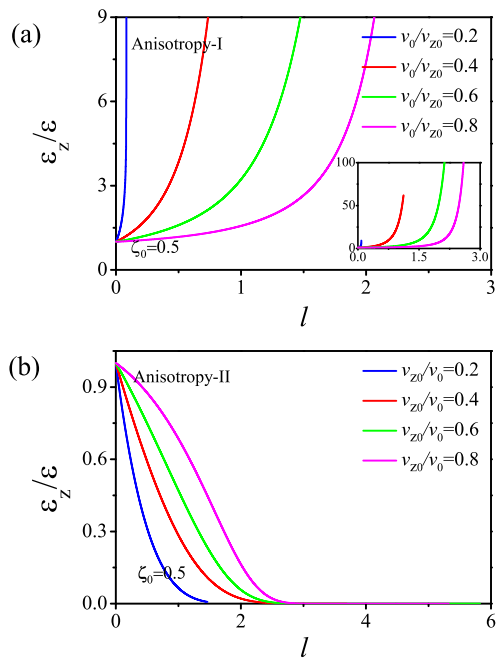


FIG. 11: (Color online) The energy-dependent evolutions of ϵ_z/ϵ are depicted with respect to the variations of initial fermion velocities, starting from (a) Anisotropy-I and (b) Anisotropy-II situations, respectively.

the initial value of tilting parameter ζ_0 , it is worth pointing out that a bigger ζ_0 is much more helpful to enhance the critical value of ϵ_z/ϵ in Anisotropy-I and increase the critical energy scale that is inversely proportional to l_c in Anisotropy-II, respectively.

In addition to checking the variation of the tilting parameter, we also examine the stability of ϵ_z/ϵ by tuning the initial anisotropy of fermion velocities. We notice from Fig. 11 that ϵ_z/ϵ exhibits a similar trend under the influence of v_0/v_{z0} as it does under the effects of ζ_0 in Fig. 10. In other words, as the energy scale decreases, ϵ_z/ϵ increases quickly and progressively vanishes while starting from the Anisotropy-I and Anisotropy-II, respectively. Besides, a stronger anisotropy of fermion velocities leads to a more quick increase or decrease.

To wrap up, the dielectric constant evolves towards the strong anisotropy in the low-energy due to the competition among various kinds of interactions. Depending on the departure from Anisotropy-I or Anisotropy-II, it can either be driven to $\epsilon_z/\epsilon \gg 1$ or $\epsilon_z/\epsilon \ll 1$. Since the strength of Coulomb interaction is inversely proportional to the dielectric constant, this indicates that the Coulomb interaction in the direction- z or direction- x, y would be considerably screened in the low-energy regime. Before going further, it is worth emphasizing that the basic behavior of g/g_0 , which characterizes the coupling strength between fermion and auxiliary bosonic field, is analogous to that of ϵ_z/ϵ and hence not shown for brevity.

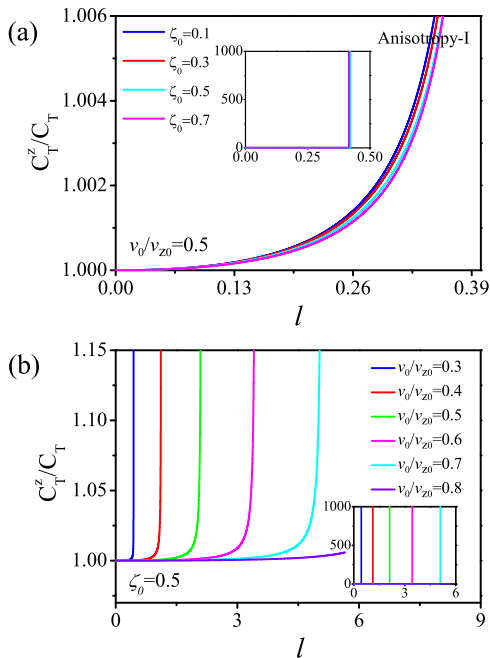


FIG. 12: (Color online) The energy-dependent evolutions of C_T^z/C_T starting from Anisotropy-I are depicted with respect to the variations of (a) ζ_0 and (b) v_0/v_{z0} , respectively.

D. Fates of phonon velocities and λ_z/λ

Next, we examine the impact of coupled interactions on phonon velocities. For the sake of simplicity, the focus is put on the velocities of transverse phonons as their longitudinal counterparts show similar behavior owing to the analogous structures of RG equations addressed in Sec. III.

With lowering the energy scale, Fig. 12 with fixed fermion velocities presents the basic tendency of C_T^z/C_T for the departure from Anisotropy-I. One can notice from Fig. 12(a) that C_T^z/C_T gradually increases and goes towards the divergence as the system approaches a critical point. Notably, these qualitative results are relatively independent of the initial value of the tilting parameter. Accordingly, we choose a specific tilting parameter $\zeta_0 = 0.5$ to examine the impact of the variation of initial anisotropy of fermion velocities as displayed in Fig. 12(b). We notice that, as long as the initial ratio of fermion velocities remains below a critical value around 0.8, the C_T^z/C_T unambiguously tends towards divergence at a critical energy scale that is increased by tuning down v_0/v_{z0} . Beyond this threshold, it is more favorable for C_T^z/C_T to converge to a finite value, slightly deviating from the isotropic case. This signals that the C_T^z/C_T prefer to display an extreme anisotropy, with the z component of the phonon velocity playing a dominant role, in contrast to the x or y component.

Compared to the case starting from Anisotropy-I, the behavior of phonon velocities in Anisotropy-II, illustrated

in Fig. 13, exhibit considerably more interesting behavior, which heavily depend on both the initial values of fermion velocities and the tilting parameter. From Fig. 13, it is evident that the low-energy fate of C_T^z/C_T is predominantly dictated by the ferocious competition between v_{z0}/v_0 and ζ_0 , which is rooted in the coupled RG equations.

To be specific, when v_{z0}/v_0 is smaller than a critical value (≈ 0.31), we can find from Fig. 13(a) that it plays a leading role in driving C_T^z/C_T towards an extreme anisotropy ($C_T^z/C_T \rightarrow 0$) at the lowest-energy limit. This behavior proves robust against variations in the value of ζ_0 . In sharp contrast, Fig. 13(c) shows that, at a moderate initial value of v_{z0}/v_0 , another form of extreme anisotropy ($C_T^z/C_T \rightarrow \infty$) would be induced upon reaching the critical energy scale. Additionally, when v_{z0}/v_0 falls within $v_{z0}/v_0 \in [0.30, 0.31]$ as presented in Fig. 13(b), we notice that the influence of v_{z0}/v_0 is subordinate to the tilting parameter. This indicates that v_{z0}/v_0 can either drive $C_T^z/C_T \rightarrow 0$ or $C_T^z/C_T \rightarrow \infty$ by varying the value of ζ_0 . It is noteworthy that, for larger values of $v_{z0}/v_0 > 0.75$, C_T^z/C_T only experiences a slight deviation from isotropy due to the concomitant effects of both v_{z0}/v_0 and ζ_0 .

To reiterate, the coupled RG equations, in tandem with the intimate competition between initial values of the fermion velocities and the tilting parameter, can drive the system towards an extreme anisotropy, where C_T^z/C_T tends towards either zero or infinity, or towards near-isotropy, where C_T^z/C_T approximately converges to one. In consequence, this signals that, as the energy scale decreases, phonons can exhibit distinct behavior, such as playing a dominant role in the z direction or xy plane as well as being nearly equivalent in all directions. In addition, we find that the qualitative behavior of λ_z/λ bears the similarity to that of C_T^z/C_T and hence not shown for brevity.

E. Fates of phonon-phonon interactions

At last, we move our attention to the low-energy tendencies of phonon-phonon interactions under the influence of all interactions in our theory.

To gain a comprehensive understanding of phonon-phonon interactions in this system, we principally need to analyze the behavior of various quantities derived from all components of the phonon-phonon couplings (5). These include V_T^{xy}/V_T^{zz} , V_T^{xz}/V_T^{zz} , V_L^{xx}/V_L^{zz} , V_L^{xy}/V_L^{zz} , V_L^{xz}/V_L^{zz} , V_T^{xx}/V_L^{xx} , V_T^{xy}/V_L^{xy} , V_T^{xz}/V_L^{xz} , and V_T^{zz}/V_L^{zz} , where the subscripts T and L denote the transverse and longitudinal phonons, respectively. In order to simplify our analysis, we can categorize them into three groups: the transverse-phonon components (V_T^{xx}/V_T^{zz} , V_T^{xy}/V_T^{zz} , V_T^{xz}/V_T^{zz}), the longitudinal-phonon components (V_L^{xx}/V_L^{zz} , V_L^{xy}/V_L^{zz} , V_L^{xz}/V_L^{zz}), and the mixed components (V_T^{xy}/V_L^{xy} , V_T^{xz}/V_L^{xz} , V_T^{zz}/V_L^{zz}). Fortunately, the numerical analysis shows that the members

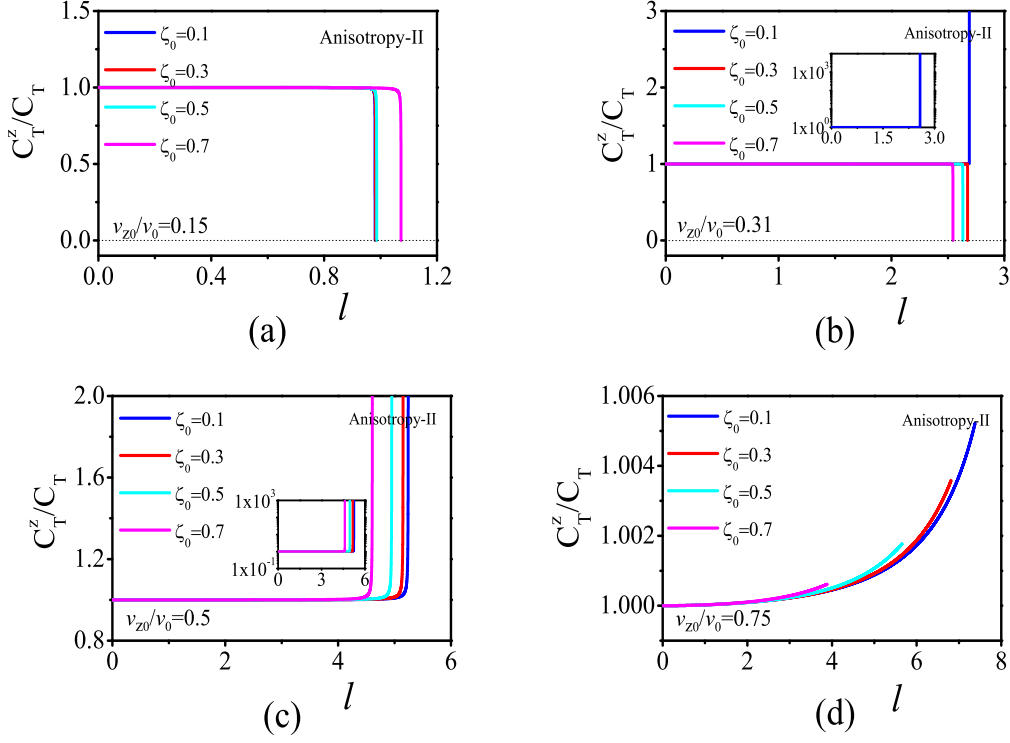


FIG. 13: (Color online) The energy-dependent evolutions of C_T^z/C_T starting from Anisotropy-II are depicted with respect to the variations of ζ_0 for fixing the fermion velocities: (a) $v_{z0}/v_0 = 0.15$, (b) $v_{z0}/v_0 = 0.31$, (c) $v_{z0}/v_0 = 0.5$, and (d) $v_{z0}/v_0 = 0.75$, respectively.

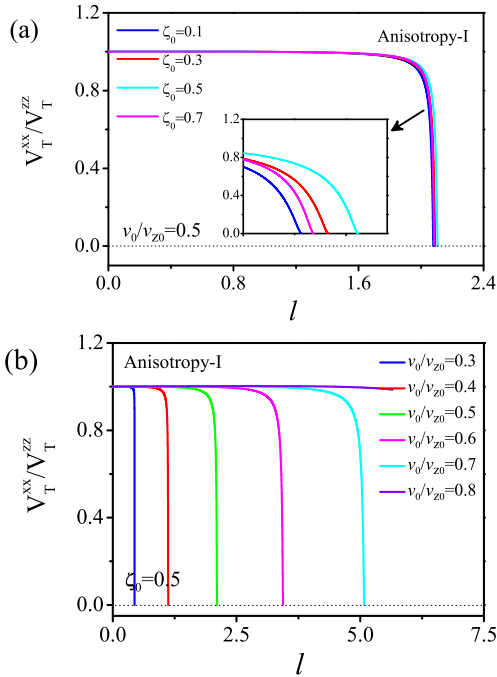


FIG. 14: (Color online) The energy-dependent evolutions of V_T^{xx}/V_T^{zz} starting from Anisotropy-I are depicted with respect to the variations of (a) ζ_0 and (b) v_0/v_{z0} , respectively.

within each category exhibit analogous tendencies as approaching the critical energy scales. Accordingly, we can effectively represent each category with a single representative behavior

Concerning the transverse-phonon components, we choose to consider the behavior of V_T^{xx}/V_T^{zz} . Starting from Anisotropy-I of fermion velocities, Fig. 14(a) manifestly shows that V_T^{xx}/V_T^{zz} slowly decreases as l increases, but then rapidly approaches zero near the critical energy. This indicates the z -component phonon interaction becomes dominant over that of x, y components. In comparison to the initial value of tilting parameter ζ_0 , which contributes only minor corrections to the basic tendencies, the critical energy scales can be considerably lowered by increasing the value of v_0/v_{z0} . In this context, V_T^{xx}/V_T^{zz} cannot be driven to the extreme anisotropy $V_T^{xx}/V_T^{zz} \rightarrow 0$. Instead, it eventually converges to a slight anisotropy, as shown in Fig. 14(b) at $v_0/v_{z0} = 0.8$. This suggests that the anisotropy of the fermion velocities plays a more pivotal crucial role in pinning down the fates of phonon interactions than the tilting parameter.

In comparison, beginning with the Anisotropy-II of fermion velocities, one can find from Fig. 15 that V_T^{xx}/V_T^{zz} bears similarities to the behavior of phonon velocities discussed in the previous subsection. If v_{z0}/v_0 is below a critical value (≈ 0.31) or takes a moderate initial value, it wins against ζ_0 , leading the system

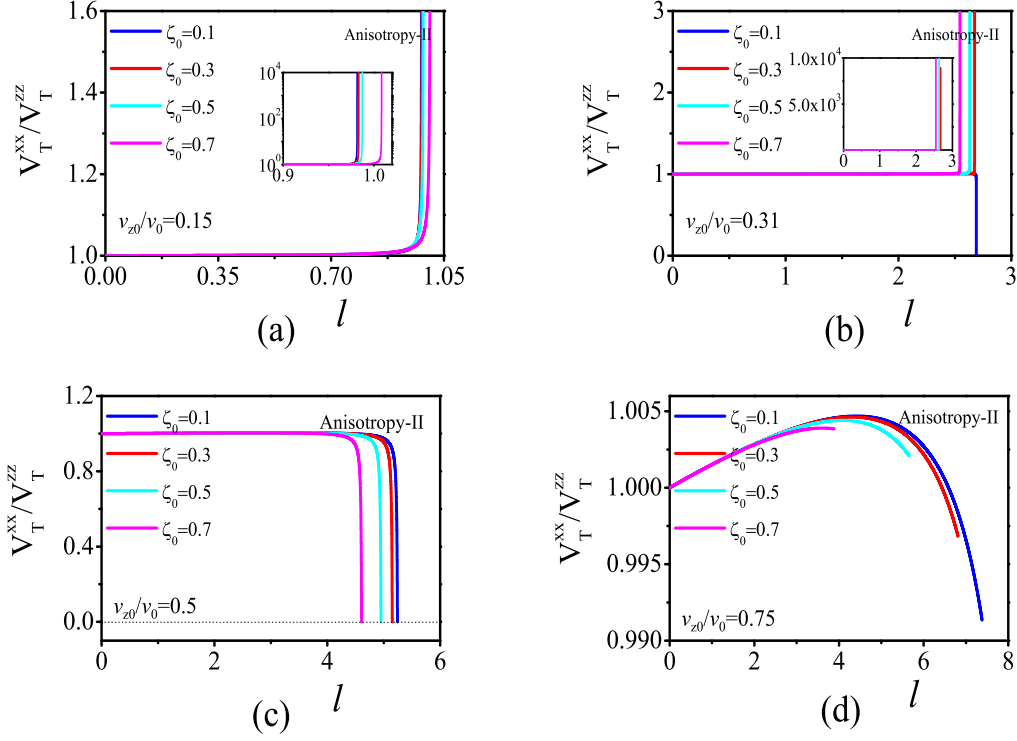


FIG. 15: (Color online) The energy-dependent evolutions of V_T^{xx}/V_T^{zz} starting from Anisotropy-II are depicted with respect to the variations of ζ_0 for fixing the fermion velocities: (a) $v_{z0}/v_0 = 0.15$, (b) $v_{z0}/v_0 = 0.31$, (c) $v_{z0}/v_0 = 0.5$, and (d) $v_{z0}/v_0 = 0.75$, respectively.

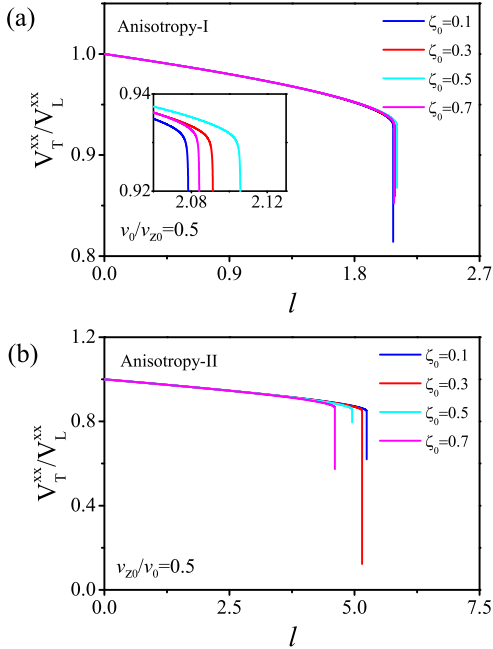


FIG. 16: (Color online) The energy-dependent evolutions of V_T^{xx}/V_L^{xx} are depicted with respect to the variations of ζ_0 , starting from (a) Anisotropy-I and (b) Anisotropy-II situations, respectively.

to an extreme anisotropy ($V_T^{xx}/V_T^{zz} \rightarrow \infty$ in the former case and $V_T^{xx}/V_T^{zz} \rightarrow 0$ in the latter case, respectively). In addition, an adequate big value of v_{z0}/v_0 renders V_T^{xx}/V_T^{zz} nearly isotropic as shown in Fig. 15(d). Otherwise, Fig. 15(b) illustrates that the influence of v_{z0}/v_0 is subordinate to ζ_0 around the critical value $v_{z0}/v_0 \approx 0.31$. This drives V_T^{xx}/V_T^{zz} to either an extreme anisotropy $V_T^{xx}/V_T^{zz} \rightarrow \infty$ or another extreme anisotropy $V_T^{xx}/V_T^{zz} \rightarrow 0$.

Since the longitudinal-phonon parts exhibit similar fates with their transverse-phonon counterparts, they are not presented here for the sake of brevity. Subsequently, our focus shifts to the mixed parts. As they share similar basic tendencies, we choose to present the behavior of V_T^{xx}/V_L^{xx} , as depicted in Fig. 16.

From Fig. 16(a) with a fixed value of $v_0/v_{z0} = 0.5$, we observe that, in the scenario initiated from Anisotropy-I, V_T^{xx}/V_L^{xx} displays a slight deviation from the isotropy as l increases and reaches a finite value at the critical energy scale. This implies that transverse-phonon and longitudinal-phonon interactions are nearly contribute equally. These basic results are similar upon varying the initial conditions. In contrast, when beginning with the Anisotropy-II, we observe in Fig. 16(b) for $v_{z0}/v_0 = 0.5$ that V_T^{xx}/V_L^{xx} is heavily dependent on the initial conditions. It decreases more significantly than its Anisotropy-I counterpart, experiencing a substantial drop at some

TABLE I: Collections of three distinct types of FPs are established based on the tendencies exhibited by interaction parameters.

Types	ζ/ζ_0	v_z/v	$\varepsilon_z/\varepsilon$	C_T^Z/C_T	V_T^{XX}/V_T^{ZZ}
Type-I	↑	↓	↓	↑	↓
Type-II	↑	↓	↓	↓	↑
Type-III	↓	↑	↑	↑	↓

optional $\zeta_0 \approx 0.3$ or $v_{z0}/v_0 \approx 0.6$, where it is driven to a state of strong anisotropy. Consequently, once we start from the Anisotropy-II, the longitudinal-phonon interactions play a more significant role than transverse-phonon interactions. Additionally, we have verified that these results are relatively stable against the change of the initial ratio of fermion velocities.

To wrap up, we figured out that the initial anisotropy of the fermion velocities plays a more crucial role in determining the fates of phonon interactions. The transverse-phonon contributions are subordinate to their longitudinal-phonon counterparts for the Anisotropy-II case, and as to the Anisotropy-I situation, both transverse- and longitudinal-phonon contributions are nearly equivalent.

V. POTENTIAL INSTABILITIES

As presented in the preceding section, the interaction parameters exhibit a number of interesting behavior dictated by the RG equations (26)-(39), which span from $l = 0$ to $l \rightarrow l_c^-$ as illustrated in Fig. 4 and Fig. 7(a). The values of all these parameters at l_c construct the fixed point (FP) in the phase space [60]. This FP generally marks a critical juncture where the potential instability from the 3D tDSM to an X phase may be induced. After examining the behavior of parameters shown in Sec. IV, we find that the fates of FPs are heavily dependent upon the tendencies of ζ/ζ_0 , v_z/v , $\varepsilon_z/\varepsilon$, C_T^Z/C_T , and V_T^{XX}/V_T^{ZZ} , which qualitatively clusters into three distinct types of FPs as presented in Table I. To simplify our analysis, we will subsequently focus exclusively on these three types of FPs and aim to identify the most favorable instabilities associated with them.

Generally, the instability serves as an indicator of certain symmetry breaking and is accompanied by the development of specific fermionic bilinears [70–75]. In order to investigate the potential instability around the FPs, we introduce the following source terms to denote the potential phase X [76, 77, 79]

$$S_{\text{sou}} = \int d\tau \int d^2\mathbf{x} \left\{ \sum_{i=1} \Delta_i^{\text{PH}} \psi^\dagger \mathcal{M}_i^{\text{PH}} \psi \right.$$

TABLE II: Potential candidates for instabilities triggered by all interactions [57, 80]. Hereby, SC, AP and CDW are abbreviations for superconductivity, anisotropy parameter and charge density wave, respectively. In addition, chiral SC₁ and SC₂ specify two distinct sorts of chiral superconducting states.

Order parameters	Fermionic bilinears	Potential phases
Δ_0^{PH}	$\mathcal{M}_0^{\text{PH}} = \sigma_0 \tau_0$	density
Δ_1^{PH}	$\mathcal{M}_1^{\text{PH}} = \sigma_0 \tau_1$	x-current
Δ_2^{PH}	$\mathcal{M}_2^{\text{PH}} = \sigma_0 \tau_2$	AP
Δ_3^{PH}	$\mathcal{M}_3^{\text{PH}} = \sigma_0 \tau_3$	CDW
Δ_0^{PP}	$\mathcal{M}_0^{\text{PP}} = \sigma_2 \tau_3$	s-wave SC
Δ_1^{PP}	$\mathcal{M}_1^{\text{PP}} = \sigma_2 \tau_1$	chiral SC ₁
Δ_2^{PP}	$\mathcal{M}_2^{\text{PP}} = \sigma_2 \tau_0$	chiral SC ₂
$\Delta_{0(0,1,3)}^{\text{PP}}$	$\mathcal{M}_{3i}^{\text{PP}} = \sigma_{(0,1,3)} \tau_2$	triplet SC

$$+ \sum_{i=1} \left[\Delta_i^{\text{PP}} \psi^\dagger \mathcal{M}_i^{\text{PP}} \psi^* + h.c. \right] \}, \quad (40)$$

where $\mathcal{M}_i^{\text{PH/PP}}$ denote the related matrices associated with the fermionic bilinears in the particle-hole and particle-particle channels, and $\Delta_i^{\text{PH/PP}}$ specify the strengths of the corresponding source terms, respectively. In our model, the primary candidates of instability and phase transition are outlined in Table II [57, 80]. To proceed, we incorporate the source terms (40) into the effective action (11) and calculate the one-loop corrections to $\Delta_i^{\text{PH/PP}}$. This yields the related RG equations for $\Delta_i^{\text{PH/PP}}$, which can be compactly expressed as

$$\frac{d\Delta_i^{\text{PH/PP}}}{dl} = \mathcal{P}(\Delta_i^{\text{PH/PP}}, v, v_z \dots), \quad (41)$$

where the detailed expressions for $\mathcal{P}(\Delta_i^{\text{PH/PP}}, v, v_z \dots)$ are provided in Appendix B. Subsequently, we are now in a suitable position to evaluate the susceptibilities accompanied by the source terms resorting to the relationship [74, 76–78]

$$\delta\chi = \frac{\partial^2 f}{\partial \Delta(0) \partial \Delta^*(0)}, \quad (42)$$

where f denotes the free energy density. With all these in hand, we can systematically study the susceptibilities of all candidates phases to identify the leading phase for phase X , which exhibits the strongest divergence of susceptibility [74].

To proceed, we notice from Eqs. (B1)-(B10), which characterizes the strengths of source terms, that certain

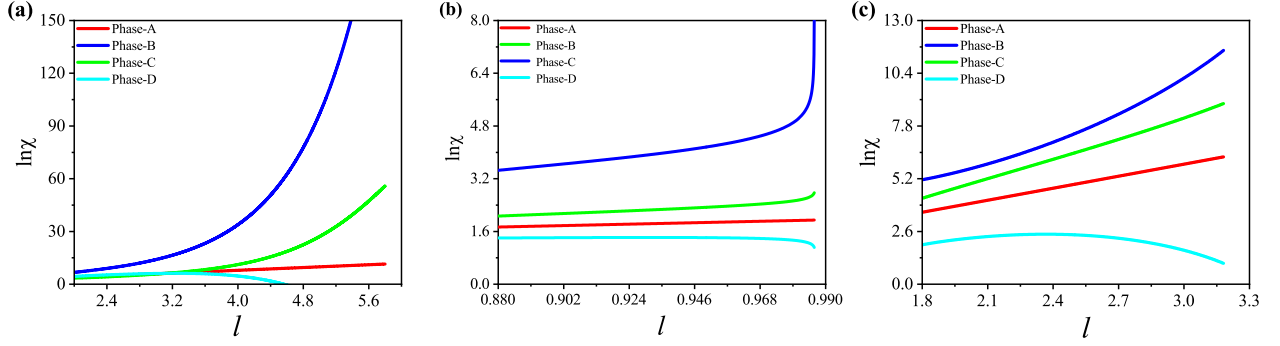


FIG. 17: (Color online) Energy-dependent susceptibilities of four different phases as approaching distinct types of FPs: (a) type-I ($v_z(0)/v(0) = 0.72$), type-II ($v_z(0)/v(0) = 0.15$), and type-III ($v(0)/v_z(0) = 0.60$) FPs, respectively.

candidates in Table II are degenerate at the one-loop level. As a consequence, it is convenient to categorize them into four cases: Phase-A (density, x -current, AP or CDW), Phase-B (s -wave SC or triplet SC₀), Phase-C (chiral SC₁ or triplet SC₁) and Phase-D (chiral SC₂ or triplet SC₃), respectively. Following a numerical analysis that combines the RG equations for both interaction parameters and $\Delta_i^{\text{PH/PP}}$, we obtain the energy-dependent susceptibilities for all four cases, as shown in Fig. 17, corresponding to the three types of FPs mentioned in Table I. Learning from Fig. 17 for several representative initial conditions, the basic results are obtained as we approach all three distinct kinds of FPs. At first, it is evident that Phase-C emerges as the leading instability once the system is driven to the type-I or type-II FP. This indicates that chiral SC₁ or triplet SC₁ becomes the dominant phase, and henceforth is the preferred candidate for the phase X displayed in Fig. 7(a)-(b). In comparison, although Phase-C is not the predominant choice among other phases around the type-III FP, it remains the optimal state for phase X as depicted in Fig. 7(c). These results are in qualitative agreement with the results in Ref. [57].

In this context, our analysis reveals the existence of an interaction-driven phase transition. The onset of instability suggests the potential emergence of critical physical implications, which we will elucidate in the next section VI.

VI. CRITICAL IMPLICATIONS AROUND THE INSTABILITIES

To proceed, we within this section examine the critical behavior of physical observables, including the density of states (DOS), compressibility, and specific heat, as the system approaches three kinds of potential FPs (instabilities) which are classified in Table I of Sec. V. In principle, it is a very challenging task to derive the analytical expressions for physical quantities directly from an interacting theory. Instead of delving into the exact expressions, a suitable and operational strategy is to extract

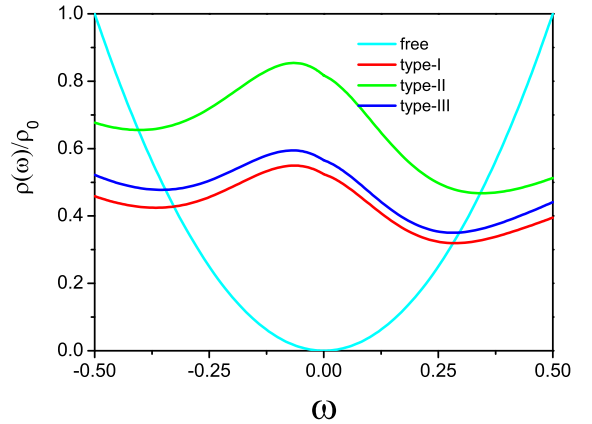


FIG. 18: (Color online) Frequency-dependent DOS $\rho(\omega)$ is depicted around around three distinct types of FPs: type-I ($v_z(0)/v(0) = 0.75$), type-II ($v_z(0)/v(0) = 0.15$), and type-III ($v(0)/v_z(0) = 0.40$), respectively. Hereby, ρ_0 is designated by $\rho_0 \equiv \rho_{\text{free}}(\zeta = 0, \omega = -0.5)$.

the physical implications from the renormalized fermionic propagator [81]. Compared to their free counterparts in Eq. (4), the fermion velocities and tilting parameter are involved in the coupled RG equations (26)-(39) and henceforth become energy-dependent. This energy dependence inherits the characteristics of the interactions, effectively capturing fundamental tendencies associated with potential instabilities. Following this strategic approach, we subsequently need to establish the relationship between the physical implications and fermion velocities as well as the tilting parameter.

A. Density of states and compressibility

At first, we consider the DOS and compressibility. After performing the analytical continuation, the renormalized retarded fermion propagator is given by [82]

$$G^{\text{ret}}(\omega, \mathbf{k}) = \{(\omega - \zeta v_z k_z)\sigma_0 + \chi[v_z k_z \sigma_z + v(k_x \sigma_x$$

$$+k_y\sigma_y)]\}/\{\omega^2 + i\text{sgn}(\omega - \zeta v_z k_z)\delta + \zeta^2 v_z^2 k_z^2 - 2\omega\zeta v_z k_z - [v_z^2 k_z^2 + v^2(k_x^2 + k_y^2)]\}, \quad (43)$$

where v, v_z and ζ are treated to be energy-dependent. The DOS of fermion quasiparticles then takes the form of

$$\frac{\rho_{\text{int}}(\omega)}{\Lambda_0^2} = \int \frac{d^3\mathbf{k}}{(2\pi)^3} \text{Tr} \left\{ -\frac{1}{\pi} \text{Im} [G^{\text{ret}}(\omega, \mathbf{k})] \right\}. \quad (44)$$

Carrying out some calculations, we arrive at

$$\frac{\rho_{\text{int}}(\omega)}{\Lambda_0^2} = \begin{cases} \int_{E,\theta,\omega} \left[\left| \omega - \frac{\zeta E(-\zeta + \cos\theta)}{1 - \zeta^2} \right| \delta(E - \omega) + \left| \omega + \frac{\zeta E(\zeta + \cos\theta)}{\zeta^2 - 1} \right| \delta \left(E - \frac{(1 - \zeta^2)\omega}{1 + \zeta^2 + 2\zeta \cos\theta} \right) \right], & \omega > 0, \\ - \int_{E,\theta,\omega} \left[\left| \omega + \frac{\zeta(\zeta - \cos\theta)E}{1 - \zeta^2} \right| \delta \left(E - \frac{(\zeta^2 - 1)\omega}{1 + \zeta^2 - 2\zeta \cos\theta} \right) + \left| \omega - \frac{\zeta(\zeta + \cos\theta)E}{1 - \zeta^2} \right| \delta(E + \omega) \right] & \omega < 0, \end{cases} \quad (45)$$

where N represents the flavor of fermions, and the notation $\int_{E,\theta,\omega}$ is designated as

$$\int_{E,\theta,\omega} \equiv \frac{N}{(2\pi)^2} \int_{e^{-l_c}}^1 dE \int_0^\pi d\theta \frac{E^2 \sin\theta}{v^2 v_z (1 - \zeta^2)\omega}. \quad (47)$$

These expressions can be reduced to

$$\frac{\rho_0(\omega)}{\Lambda_0^2} = \frac{N\omega^2}{\pi^2 v^2 v_z (1 - \zeta^2)^2}. \quad (48)$$

in the noninteracting case.

As to the compressibility, it is originally defined as $\kappa = \partial V / \partial F$ [83], where V and F represent the volume and compression force, respectively. Hereby, it is more convenient to introduce the chemical potential μ and then calculate using $\kappa = \partial n / \partial \mu$, where n is the number of particles per area directly associated with the DOS [81, 84]. After performing the necessary calculations, we are left with

$$\frac{\kappa_{\text{int}}(\mu)}{\Lambda_0} = \begin{cases} \int_{E,\theta,\mu} \left[\left| \frac{\zeta(\zeta - \cos\theta)E}{1 - \zeta^2} - 2\mu \right| \delta \left(E - \frac{2(1 - \zeta^2)\mu}{1 + \zeta^2 - 2\zeta \cos\theta} \right) + \left| 2\mu + \frac{\zeta(\zeta + \cos\theta)E}{1 - \zeta^2} \right| \delta(E - 2\mu) \right], & \mu > 0, \\ \int_{E,\theta,\mu} \left[\left| \frac{\zeta(\zeta - \cos\theta)E}{1 - \zeta^2} - 2\mu \right| \delta(E + 2\mu) + \left| 2\mu + \frac{\zeta(\zeta + \cos\theta)E}{1 - \zeta^2} \right| \delta \left(E + \frac{2(1 - \zeta^2)\mu}{1 + \zeta^2 + 2\zeta \cos\theta} \right) \right], & \mu < 0, \end{cases} \quad (49)$$

where $\int_{E,\theta,\mu}$ is introduced as

$$\int_{E,\theta,\mu} \equiv \frac{N}{8\pi^2} \int_{e^{-l_c}}^1 dE \int_0^\pi d\theta \frac{E^2 \sin\theta}{v^2 v_z (1 - \zeta^2)\mu}. \quad (51)$$

Similarly, the free-limit expression can be derived by taking $l_c \rightarrow \infty$, with v, v_z, ζ assumed as constants.

With the above information in hand, we delve into the behavior of DOS and κ both influenced by the interactions. By combining Eqs. (45)-(46) and (49)-(50) with the RG equations (26)-(39), their basic tendencies are obtained as we approach three distinct kinds of instabilities. The behavior of DOS is illustrated in Fig. 18. In the absence of interactions and tilting parameter, the DOS exhibits a parabolic frequency dependence, $\rho_0(\omega) \propto \omega^2$, and hence it vanishes precisely at the Dirac point. In sharp contrast, approaching the three types of identified instabilities introduces the interaction contributions that

render the DOS a non-zero finite value at $\omega = 0$. This is qualitatively distinct from the free case and the nonzero tilting parameter further amplifies the departure by inducing an asymmetry for $\omega > 0$ and $\omega < 0$. Away from $\omega = 0$, the intimate competition between the interactions and thermal fluctuations governs the behavior of DOS. We can find that the DOS decreases at first and then ascends around $|\omega| \gtrsim \omega_c \approx 0.25$. This indicates that below the critical frequency ω_c , the thermal fluctuations are subordinate to the interactions, while above it, the thermal fluctuations dominate. In addition, although the DOS tendencies near all three types of instabilities are similar, the type-II instability leads to a little more corrections compared to the other two types.

Regarding the compressibility denoted as κ , Fig. 19 shows the μ -dependent evolution of κ in the vicinity of three types of instabilities. In the absence of interactions

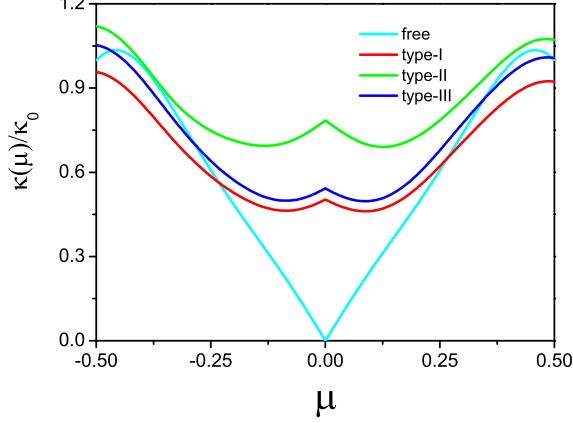


FIG. 19: (Color online) Behavior of $\kappa(\mu)$ around three distinct types of FPs: type-I ($v_z(0)/v(0) = 0.75$), type-II ($v_z(0)/v(0) = 0.15$), and type-III ($(v(0)/v)_z(0) = 0.40$), respectively. Hereby, κ_0 is designated by $\kappa_0 \equiv \kappa_{\text{free}}(\zeta = 0, \mu = -0.5)$.

and tilting parameters, the compressibility in the free case, $\kappa_{\text{free},\zeta=0}(\mu)$, exhibits a nearly linear dependence on μ and becomes incompressible at $\mu = 0$, which is consistent with the behavior of the free DOS. However, once the contributions from the interactions and tilting parameter are taken into account, the behavior of κ under-

goes qualitative changes for $\mu \leq \mu_c \approx 0.25$. It becomes much more compressible, reaching its maximum value at $\mu = 0$. Subsequently, the compressibility increases at $\mu > \mu_c$ and exhibits a similar tendency to the free case for sufficiently large μ . This change would arise from the intricate interplay between interactions and thermal fluctuations. Besides, it is observed that κ experiences more corrections near the type-II instability. Moreover, we notice that the tilting parameter seems to introduce only minor corrections with opposite signs to κ .

B. Specific heat

Next, we turn our attention to the specific heat of the quasiparticle. The free energy density $f(T)$ can be written as

$$f(T) = -\frac{T}{V} \ln Z, \quad (52)$$

where the partition function is associated with [85]

$$Z = \prod_{n,k,\alpha} \int [d(i\psi_{\alpha,n}^\dagger)] [d\psi_{\rho,n}] e^{S_0}, \quad (53)$$

with S_0 denoting the fermionic component of our theory. After long but straightforward calculations, we finally obtain

$$\begin{aligned} \frac{f(T)}{\Lambda_0^4} = & -\frac{T}{4\pi^2} \int_{e^{-l_c}}^1 dE \int_0^\pi d\theta \frac{E^2 \sin \theta (1 - \zeta \cos \theta)}{v^2 v_z (1 - \zeta^2)^2} \left[\ln(1 + e^{-\sqrt{x^+}}) + \ln(1 + e^{-\sqrt{y^+}}) \right] \\ & -\frac{T}{4\pi^2} \int_{e^{-l_c}}^1 dE \int_0^\pi d\theta \frac{E^2 \sin \theta (1 + \zeta \cos \theta)}{v^2 v_z (1 - \zeta^2)^2} \left[\ln(1 + e^{-\sqrt{x^-}}) + \ln(1 + e^{-\sqrt{y^-}}) \right]. \end{aligned} \quad (54)$$

In this expression, we utilize the transformations $E \rightarrow E/\Lambda_0$, $T \rightarrow T/\Lambda_0$, and define x^\pm, y^\pm as

$$x^+ \equiv \frac{\mathcal{N}_- E^2}{(1 - \zeta^2)^2 T^2}, \quad (55)$$

$$y^+ \equiv \frac{(\zeta^2 + 1 - 2\zeta \cos \theta)^2 E^2}{\mathcal{N}_- T^2}, \quad (56)$$

$$x^- \equiv \frac{\mathcal{N}_+ E^2}{(1 - \zeta^2)^2 T^2}, \quad (57)$$

$$y^- \equiv \frac{(\zeta^2 + 1 + 2\zeta \cos \theta)^2 E^2}{\mathcal{N}_+ T^2}, \quad (58)$$

with \mathcal{N}_\mp denominated as

$$\begin{aligned} \mathcal{N}_\mp = & \zeta^2(1 + \zeta^2) \mp 2\zeta(1 + \zeta^2) \cos \theta + (1 + \zeta^2 \cos(2\theta)) \\ & + \sqrt{2\zeta^2 (\zeta \mp \cos \theta)^2 [\zeta^2 \mp 4\zeta \cos \theta + \zeta^2 \cos(2\theta) + 2]}. \end{aligned}$$

In consequence, the specific heat can be derived as

$$C_V(T) = -T \frac{\partial^2 f(T)}{\partial T^2}. \quad (59)$$

Once again, the free limit C_V^0 can be obtained by taking $l_c \rightarrow \infty$ and considering v, v_z, ζ as specific constants.

After taking into account the RG equations of interaction parameters and the expression for C_V (59), the numerical results for C_V are illustrated in Fig. 20 in the vicinity of three distinct kinds of instabilities. At first, compared to the free case $C_V^0(T) \propto T^2$ in the absence of interactions and tilting parameter, we notice that the intimate interplay between the tilting parameter and interactions establishes close relationships and constraints among the low-energy quasiparticles. As a result, this interaction-induced effect on the specific heat leads to a slight deviation of the renormalized $C_V(T)$ from the T^2

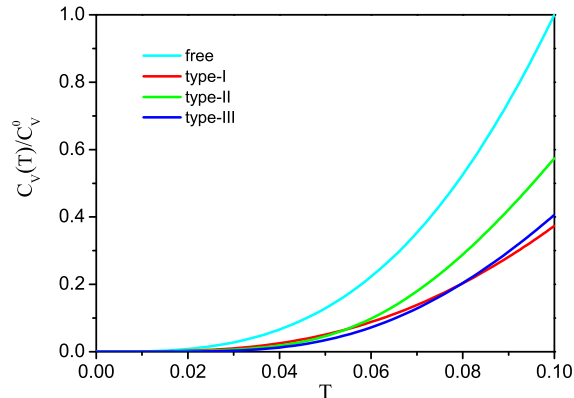


FIG. 20: (Color online) Temperature-dependent evolutions of specific heat $C_V(T)$ around three distinct types of FPs: type-I ($v_z(0)/v(0) = 0.75$), type-II ($v_z(0)/v(0) = 0.15$), and type-III ($v(0)/v_z(0) = 0.40$), respectively. Hereby, C_{V0} is designated by $C_{V0} \equiv C_V^{\text{free}}(\zeta = 0, T = 0.1)$.

dependence, indicative of non-Fermi liquid behavior [81]. In addition, although C_V is suppressed as we approach all three kinds of instabilities, it is unequivocally evident from Fig. 20 that the specific heat is less reduced in the type-II case compared to the other two cases. This is qualitative in agreement with the basic tendencies of the DOS and compressibility presented in Sec. VIA.

To be brief, all these physical implications surrounding the potential instabilities would be of particular help to delve deeper into the study of more quantities of the related tilted materials.

VII. SUMMARY

In summary, we study the low-energy physics of a type-I 3D tDSM by adopting the powerful RG method [58–60], which helps us to unbiasedly treat all physical ingredients, including the Coulomb interactions and electron-phonon coupling as well as phonon-phonon interactions. By considering all one-loop corrections, we derived the coupled RG equations for all relevant parameters. After performing the numerical analysis, we systematically presented the low-energy behavior of these interactions and their influence on potential instabilities and physical properties.

To begin with, we examine the fate of the tilting parameter and observe two distinct scenarios depending on the initial anisotropy of fermion velocities. To ensure the self-consistency of our theory, we only focus on the first scenario, as shown in Fig. 7(a). Within this scenario, we find that the anisotropy of fermion velocities is primarily dependent on its initial value but is insensitive to the strength of the tilting parameter. Notably, this anisotropy may exhibit an increase, decrease, or remain nearly constant in the low-energy regime. Regarding the

ratio of dielectric constant ϵ_z/ϵ , it always flows towards either extreme anisotropy, i.e., $\epsilon_z/\epsilon \gg 1$ or $\epsilon_z/\epsilon \ll 1$, when starting from Anisotropy-I or Anisotropy-II, respectively. This suggests the screening of Coulomb interaction in the direction- z or direction- x, y . Furthermore, the fate of g/g_0 is analogous to that of ϵ_z/ϵ . Compared to the ϵ_z/ϵ , we notice that both the phonon velocities and phonon-phonon interactions can either flow towards approximate isotropy or bear similarities to the extreme anisotropy observed in ϵ_z/ϵ in the low-energy regime. Analogously, the anisotropy of electron-phonon interactions λ_z/λ shares the similar tendency of phonon velocities C_T^z/C_T .

Subsequently, we systematically investigate the tendencies of all interaction parameters, which give rise to three distinct types of FPs as displayed in Table I. After introducing the source terms for the potential symmetry breakings and comparing their susceptibilities accessing the FPs, we find that there exists an interaction-driven phase transition around the FPs, with either Phase-B or Phase-C emerged as the preferred leading instability. Additionally, we delve into the critical properties of physical quantities, including the density of states and compressibility as well as specific heat, as the system approaches these three distinct types of FPs. In sharp contrast to their non-interacting counterparts, they exhibit very different behavior, particularly in the proximity of the Dirac point. Notably, they deviate slightly from the scope of Fermi-liquid behavior. To recapitulate, we expect all these results will be helpful to provide relevant clues for investigating the fascinating behavior of 3D tDSM and exploring other related tilted materials in the future.

ACKNOWLEDGEMENTS

We thank Y. H. Zhai, W. Liu and X. Z. Chu for useful discussions. J.W. was partially supported by the National Natural Science Foundation of China under Grant No. 11504360.

Appendix A: Collections of one-loop corrections

After long calculations, we hereby present the one-loop corrections to all vertex couplings in our effective theory (11) as illustrated in Fig. 21. These corrections arise from the interplay among the Coulomb interaction, electron-phonon interaction, and phonon-phonon interaction, which can be formally expressed as follows,

$$\delta g = \mathcal{B}gl, \quad (\text{A1})$$

$$\delta \lambda = \mathcal{D}\lambda l, \quad (\text{A2})$$

$$\delta \lambda_z = \mathcal{D}_z \lambda_z l, \quad (\text{A3})$$

$$\delta V_{T,L}^{ij} = V_{T,L}^{ij} \mathcal{F}_{T,L}^{i,j} l, \text{ with } i, j = x, y, z, \quad (\text{A4})$$

Here, we have neglected the unimportant constant terms for clarity. All related coefficients that are involved in

both Eqs. (A1)-(A4) and RG equations (26)-(39) are nominated in the following.

As to the coefficients \mathcal{A}_1 and \mathcal{A}_2 , we have

$$\mathcal{A}_1 \equiv \int_0^\pi d\theta (\mathcal{A}_{11} - \mathcal{A}_{12}), \quad (\text{A5}) \quad \text{with } \mathcal{A}_{11}, \mathcal{A}_{12}, \mathcal{A}_{21}, \text{ and } \mathcal{A}_{22} \text{ being}$$

$$\mathcal{A}_2 \equiv \int_0^\pi d\theta (\mathcal{A}_{21} + \mathcal{A}_{22}), \quad (\text{A6})$$

$$\begin{aligned} \mathcal{A}_{11} \equiv & \frac{-\eta_\zeta(1-\zeta^2)g^2\epsilon}{2\pi v^4 v_z} \frac{(1-\zeta^2)\sin^3\theta}{\left[\epsilon\frac{(1-\zeta^2)\sin^2\theta}{v^2} + \epsilon_z\left(\frac{\cos\theta-|\zeta|}{v_z}\right)^2\right]^2} + \frac{\eta_\zeta(1-\zeta^2)}{16\pi^2 v^4 v_z} \frac{\lambda^2 \mathcal{J}\left[\frac{(1-\zeta^2)\sin^2\theta}{v^2} + \frac{2(\cos\theta-|\zeta|)^2}{v_z^2}\right] \sin\theta}{(1-|\zeta|\cos\theta)^2 \left[(1-|\zeta|\cos\theta + \mathcal{I})^2 - \zeta^2(\cos\theta-|\zeta|)^2\right]^2} \\ & \times \left\{ 2(1-|\zeta|\cos\theta) \left[(1-2\zeta^2)(\cos\theta-|\zeta|)^2 + (1-\zeta^2)\sin^2\theta \right] \mathcal{I} + (1-\zeta^2)^2 \left[(\cos\theta-|\zeta|)^2 + \sin^2\theta \right]^2 \right. \\ & + (1-\zeta^2) \left[(\cos\theta-|\zeta|)^2 + \sin^2\theta \right] \mathcal{I}^2 + 2\zeta^2(\cos\theta-|\zeta|)^2 \left[3(1-|\zeta|\cos\theta)^2 + 4(1-|\zeta|\cos\theta)\mathcal{I} + \mathcal{I}^2 - \zeta^2(\cos\theta-|\zeta|)^2 \right] \\ & + \frac{(1-\zeta^2)[(\cos\theta-|\zeta|)^2 + (1-v)\sin^2\theta]}{\mathcal{I}} \left. \left\{ 2(1-|\zeta|\cos\theta)^3 + [5(1-|\zeta|\cos\theta)^2 - \zeta^2(\cos\theta-|\zeta|)^2] \mathcal{I} \right. \right. \\ & \left. \left. + 4(1-|\zeta|\cos\theta)\mathcal{I}^2 + \mathcal{I}^3 \right\} \right\} + \frac{\eta_\zeta(1-\zeta^2)^2}{16\pi^2 v^4 v_z} \frac{\lambda \mathcal{J}\left[\frac{\lambda_z(\cos\theta-|\zeta|)^2}{v_z} + \frac{\lambda(1-\zeta^2)\sin^2\theta}{4v}\right] \sin^3\theta}{(1-|\zeta|\cos\theta)^2 \left[(1-|\zeta|\cos\theta + \mathcal{I})^2 - \zeta^2(\cos\theta-|\zeta|)^2\right]^2 \mathcal{I}} \\ & \times \left\{ 2(1-|\zeta|\cos\theta)^3 + [5(1-|\zeta|\cos\theta)^2 - \zeta^2(\cos\theta-|\zeta|)^2] \mathcal{I} + 4(1-|\zeta|\cos\theta)\mathcal{I}^2 + \mathcal{I}^3 \right\}, \end{aligned} \quad (\text{A7})$$

$$\begin{aligned} \mathcal{A}_{12} \equiv & \frac{\eta_\zeta(1-\zeta^2)}{16\pi^2 v^4 v_z} \frac{\frac{-2\mathcal{J}\lambda_z^2(\cos\theta-|\zeta|)^2}{v_z^2} \sin\theta}{(1-|\zeta|\cos\theta)^2 \left[(1-|\zeta|\cos\theta + \mathcal{I}')^2 - \zeta^2(\cos\theta-|\zeta|)^2\right]^2} \left\{ 2(1-|\zeta|\cos\theta) \left[(1-2\zeta^2)(\cos\theta-|\zeta|)^2 \right. \right. \\ & \left. \left. + (1-\zeta^2)\sin^2\theta \right] \mathcal{I}' + (1-\zeta^2)^2 \left[(\cos\theta-|\zeta|)^2 + \sin^2\theta \right]^2 + (1-\zeta^2) \left[(\cos\theta-|\zeta|)^2 + \sin^2\theta \right] \mathcal{I}'^2 \right. \\ & \left. + 2\zeta^2(\cos\theta-|\zeta|)^2 \left[3(1-|\zeta|\cos\theta)^2 + 4(1-|\zeta|\cos\theta)\mathcal{I}' + \mathcal{I}'^2 - \zeta^2(\cos\theta-|\zeta|)^2 \right] + \frac{(1-\zeta^2)[(\cos\theta-|\zeta|)^2 + (1-v)\sin^2\theta]}{\mathcal{I}'} \right. \\ & \left. \times \left\{ 2(1-|\zeta|\cos\theta)^3 + [5(1-|\zeta|\cos\theta)^2 - \zeta^2(\cos\theta-|\zeta|)^2] \mathcal{I}' + 4(1-|\zeta|\cos\theta)\mathcal{I}'^2 + \mathcal{I}'^3 \right\} \right\} \\ & - \frac{\eta_\zeta(1-\zeta^2)^2}{16\pi^2 v^4 v_z} \frac{2\lambda \mathcal{J}\left[\frac{\lambda_z(\cos\theta-|\zeta|)^2}{v_z} + \frac{\lambda(1-\zeta^2)\sin^2\theta}{4v}\right] \sin^3\theta}{(1-|\zeta|\cos\theta)^2 \left[(1-|\zeta|\cos\theta + \mathcal{I}')^2 - \zeta^2(\cos\theta-|\zeta|)^2\right]^2 \mathcal{I}'} \\ & \times \left\{ 2(1-|\zeta|\cos\theta)^3 + [5(1-|\zeta|\cos\theta)^2 - \zeta^2(\cos\theta-|\zeta|)^2] \mathcal{I}' + 4(1-|\zeta|\cos\theta)\mathcal{I}'^2 + \mathcal{I}'^3 \right\}, \end{aligned} \quad (\text{A8})$$

$$\begin{aligned} \mathcal{A}_{21} \equiv & \frac{-\eta_\zeta(1-\zeta^2)\epsilon_z g^2}{\pi v^2 v_z^3} \frac{(\cos\theta-|\zeta|)^2 \sin\theta}{\left[\epsilon\frac{(1-\zeta^2)\sin^2\theta}{v^2} + \epsilon_z\left(\frac{\cos\theta-|\zeta|}{v_z}\right)^2\right]^2} + \frac{\eta_\zeta(1-\zeta^2)}{16\pi^2 v^2 v_z^3} \frac{2\lambda_z^2 \mathcal{J}\left[\frac{(1-\zeta^2)\sin^2\theta}{v^2}\right] \sin\theta}{(1-|\zeta|\cos\theta)^2 \left[(1-|\zeta|\cos\theta + \mathcal{I})^2 - \zeta^2(\cos\theta-|\zeta|)^2\right]^2} \\ & \times \left\{ (1-\zeta^2)^2 \left[(\cos\theta-|\zeta|)^2 + \sin^2\theta \right]^2 + 2(1-|\zeta|\cos\theta) \left[(1-2\zeta^2)(\cos\theta-|\zeta|)^2 + (1-\zeta^2)\sin^2\theta \right] \mathcal{I} \right. \\ & \left. + (1-\zeta^2) \left[(\cos\theta-|\zeta|)^2 + \sin^2\theta \right] \mathcal{I}^2 + 2\zeta^2(1-v_z)(\cos\theta-|\zeta|)^2 \left[3(1-|\zeta|\cos\theta)^2 + 4(1-|\zeta|\cos\theta)\mathcal{I} + \mathcal{I}^2 - \zeta^2(\cos\theta-|\zeta|)^2 \right] \right. \\ & \left. + \frac{(1-\zeta^2)[(1+2v_z)(\cos\theta-|\zeta|)^2 + \sin^2\theta]}{\mathcal{I}} \left\{ 2(1-|\zeta|\cos\theta)^3 + [5(1-|\zeta|\cos\theta)^2 - \zeta^2(\cos\theta-|\zeta|)^2] \mathcal{I} + \mathcal{I}^3 + 4(1-|\zeta|\cos\theta)\mathcal{I}^2 \right\} \right\} \\ & - \frac{\eta_\zeta(1-\zeta^2)}{16\pi^2 v^2 v_z^3} \frac{\mathcal{J}v_z(1-\zeta^2)\lambda\lambda_z \sin^2\theta(\cos\theta-|\zeta|)^2 \sin\theta}{(1-|\zeta|\cos\theta)^2 \left[(1-|\zeta|\cos\theta + \mathcal{I})^2 - \zeta^2(\cos\theta-|\zeta|)^2\right]^2} \left\{ \zeta^2 \left[3(1-|\zeta|\cos\theta)^2 + 4(1-|\zeta|\cos\theta)\mathcal{I} + \mathcal{I}^2 \right. \right. \\ & \left. \left. - \zeta^2(\cos\theta-|\zeta|)^2 \right] - \frac{1}{\mathcal{I}} \left\{ 2(1-|\zeta|\cos\theta)^3 + [5(1-|\zeta|\cos\theta)^2 - \zeta^2(\cos\theta-|\zeta|)^2] \mathcal{I} + 4(1-|\zeta|\cos\theta)\mathcal{I}^2 + \mathcal{I}^3 \right\} \right\}, \end{aligned} \quad (\text{A9})$$

$$\begin{aligned} \mathcal{A}_{22} \equiv & \frac{\eta_\zeta(1-\zeta^2)}{16\pi^2 v^2 v_z^3} \frac{2\mathcal{J}\left[-\frac{\lambda^2(1-\zeta^2)\sin^2\theta}{v^2} + \frac{\lambda_z^2(\cos\theta-|\zeta|)^2}{v_z^2}\right] \sin\theta}{(1-|\zeta|\cos\theta)^2 \left[(1-|\zeta|\cos\theta + \mathcal{I}')^2 - \zeta^2(\cos\theta-|\zeta|)^2\right]^2} \left\{ (1-\zeta^2)^2 \left[(\cos\theta-|\zeta|)^2 + \sin^2\theta \right]^2 \right. \\ & \left. + 2(1-|\zeta|\cos\theta) \left[(1-2\zeta^2)(\cos\theta-|\zeta|)^2 + (1-\zeta^2)\sin^2\theta \right] \mathcal{I}' + (1-\zeta^2) \left[(\cos\theta-|\zeta|)^2 + \sin^2\theta \right] \mathcal{I}'^2 + 2\zeta^2(1-v_z) \right. \\ & \left. \times (\cos\theta-|\zeta|)^2 \left[3(1-|\zeta|\cos\theta)^2 + 4(1-|\zeta|\cos\theta)\mathcal{I}' + \mathcal{I}'^2 - \zeta^2(\cos\theta-|\zeta|)^2 \right] + \frac{(1-\zeta^2)[(1+2v_z)(\cos\theta-|\zeta|)^2 + \sin^2\theta]}{\mathcal{I}'} \right\} \end{aligned}$$

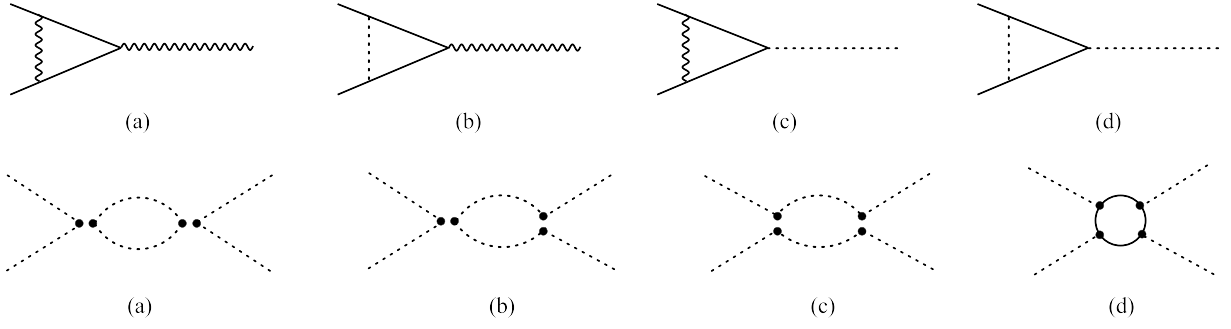


FIG. 21: One-loop corrections to (a)-(b) the Coulomb interaction, (c)-(d) the electron-phonon interaction, and (e)-(h) the phonon-phonon interactions, respectively (the solid, wavy, and dashed lines denote the free fermionic, auxiliary bosonic, and phonon propagators).

$$\begin{aligned}
& \times \left\{ 2(1 - |\zeta| \cos \theta)^2 + [5(1 - |\zeta| \cos \theta)^2 - \zeta^2 (\cos \theta - |\zeta|)^2] \mathcal{I}' + 4(1 - |\zeta| \cos \theta) \mathcal{I}'^2 + \mathcal{I}'^3 \right\} + \frac{\eta_\zeta (1 - \zeta^2)}{16\pi^2 v^2 v_z^3} \\
& \times \frac{2\mathcal{J}(1 - \zeta^2) \lambda \lambda_z v_z \sin^2 \theta (\cos \theta - |\zeta|)^2 \sin \theta}{(1 - |\zeta| \cos \theta)^2 [(1 - |\zeta| \cos \theta + \mathcal{I}')^2 - \zeta^2 (\cos \theta - |\zeta|)^2]^2} \left\{ \zeta^2 [3(1 - |\zeta| \cos \theta)^2 + 4(1 - |\zeta| \cos \theta) \mathcal{I}' + \mathcal{I}'^2 - \zeta^2 (\cos \theta - |\zeta|)^2] \right. \\
& \left. - \frac{1}{\mathcal{I}'} \left\{ 2(1 - |\zeta| \cos \theta)^3 + [5(1 - |\zeta| \cos \theta)^2 - \zeta^2 (\cos \theta - |\zeta|)^2] \mathcal{I}' + 4(1 - |\zeta| \cos \theta) \mathcal{I}'^2 + \mathcal{I}'^3 \right\} \right\}, \quad (\text{A10})
\end{aligned}$$

and for the coefficients \mathcal{A}_0 and \mathcal{A}_3 ,

$$\begin{aligned}
\mathcal{A}_0 &= -\frac{\eta_\zeta (1 - \zeta^2)}{4\pi^2 v^2 v_z} \int_0^\pi d\theta \sin \theta \left\{ \frac{[(2\lambda^2 + \lambda_z^2)(1 - |\zeta| \cos \theta) - \mathcal{J}']}{\left\{ [(1 - |\zeta| \cos \theta) + \mathcal{I}']^2 - \zeta^2 (\cos \theta - |\zeta|)^2 \right\} \mathcal{I}'} + \frac{\mathcal{J}'(1 - |\zeta| \cos \theta)}{\left\{ [(1 - |\zeta| \cos \theta) + \mathcal{I}']^2 - \zeta^2 (\cos \theta - |\zeta|)^2 \right\} \mathcal{I}'} \right\} \quad (\text{A11}) \\
\mathcal{A}_3 &\equiv \frac{\eta_\zeta (1 - \zeta^2)}{4\pi^2 v^2 v_z} \int_0^\pi d\theta \left\{ \frac{\sin \theta [(2\lambda^2 + \lambda_z^2) - \lambda^2 \mathcal{J} \frac{(\infty - \zeta^\epsilon) \sin^\epsilon \theta}{\zeta^\epsilon} + \lambda_z^2 \frac{(\cos \theta - |\zeta|)^\epsilon}{\zeta^\epsilon}]}{(1 - |\zeta| \cos \theta)^2 [(1 - |\zeta| \cos \theta + \mathcal{I}')^2 - \zeta^2 (\cos \theta - |\zeta|)^2]^2} \left\{ -\frac{1}{2} \left\{ (1 - \zeta^2)^2 [(\cos \theta - |\zeta|)^2 + \sin^2 \theta]^2 \right. \right. \right. \\
& + 2(1 - |\zeta| \cos \theta) [(1 - 2\zeta^2)(\cos \theta - |\zeta|)^2 + (1 - \zeta^2) \sin^2 \theta] \mathcal{I} + (1 - \zeta^2) [(\cos \theta - |\zeta|)^2 + \sin^2 \theta] \mathcal{I}^2 \left. \left. \left. \right\} + (1 - \zeta^2)(\cos \theta - |\zeta|)^2 \right. \right. \\
& \times [3(1 - |\zeta| \cos \theta)^2 + 4(1 - |\zeta| \cos \theta) \mathcal{I} + \mathcal{I}^2 - \zeta^2 (\cos \theta - |\zeta|)^2] + \frac{(1 - \zeta^2) [\sin^2 \theta - (\cos \theta - |\zeta|)^2]}{2\mathcal{I}} \left. \left. \left. \right\} 2(1 - |\zeta| \cos \theta)^3 \right. \right. \\
& + [5(1 - |\zeta| \cos \theta)^2 - \zeta^2 (\cos \theta - |\zeta|)^2] \mathcal{I} + 4(1 - |\zeta| \cos \theta) \mathcal{I}^2 + \mathcal{I}^3 \left. \left. \left. \right\} \right\} + \frac{\sin \theta \mathcal{J}'}{(1 - |\zeta| \cos \theta)^2 [(1 - |\zeta| \cos \theta + \mathcal{I}')^2 - \zeta^2 (\cos \theta - |\zeta|)^2]^2} \\
& \times \left\{ -\frac{1}{2} \left\{ (1 - \zeta^2)^2 [(\cos \theta - |\zeta|)^2 + \sin^2 \theta]^2 + 2(1 - |\zeta| \cos \theta) [(1 - 2\zeta^2)(\cos \theta - |\zeta|)^2 + (1 - \zeta^2) \sin^2 \theta] \mathcal{I}' \right. \right. \\
& + (1 - \zeta^2) [(\cos \theta - |\zeta|)^2 + \sin^2 \theta] \mathcal{I}'^2 \left. \left. \right\} + (1 - \zeta^2)(\cos \theta - |\zeta|)^2 \times [3(1 - |\zeta| \cos \theta)^2 + 4(1 - |\zeta| \cos \theta) \mathcal{I}' + \mathcal{I}'^2 - \zeta^2 (\cos \theta - |\zeta|)^2] \right. \\
& \left. + \frac{(1 - \zeta^2) [\sin^2 \theta - (\cos \theta - |\zeta|)^2]}{2\mathcal{I}'} \left\{ 2(1 - |\zeta| \cos \theta)^3 + [5(1 - |\zeta| \cos \theta)^2 - \zeta^2 (\cos \theta - |\zeta|)^2] \mathcal{I}' + 4(1 - |\zeta| \cos \theta) \mathcal{I}'^2 + \mathcal{I}'^3 \right\} \right\}. \quad (\text{A12})
\end{aligned}$$

With respect to the other coefficients, we get

$$\begin{aligned}
\mathcal{B} &\equiv -\int_0^\pi d\theta \frac{\sin \theta}{(1 - |\zeta| \cos \theta)^2 [(1 - |\zeta| \cos \theta + \mathcal{I}')^2 - \zeta^2 (\cos \theta - |\zeta|)^2]^2} \frac{\eta_\zeta (1 - \zeta^2)}{16\pi^2 v^2 v_z} \left\{ 2[(2\lambda^2 + \lambda_z^2) - \mathcal{J}'] \right. \\
& \times \left\{ \mathcal{I}'^2 (1 - \zeta^2) [(\cos \theta - |\zeta|)^2 + \sin^2 \theta] + (1 - \zeta^2)^2 [(\cos \theta - |\zeta|)^2 + \sin^2 \theta]^2 + 2\mathcal{I}'(1 - |\zeta| \cos \theta) [(1 - 2\zeta^2)(\cos \theta - |\zeta|)^2 \right. \\
& \left. + (1 - \zeta^2) \sin^2 \theta] \right\} - \frac{1}{2\mathcal{I}'} \left\{ \mathcal{I}'^3 + 2(1 - |\zeta| \cos \theta)^3 + 4\mathcal{I}'^2(1 - |\zeta| \cos \theta) + \mathcal{I}' [5(1 - |\zeta| \cos \theta)^2 - \zeta^2 (\cos \theta - |\zeta|)^2] \right\} \\
& \times \left\{ 2\lambda^2 (1 - \zeta^2) \sin^2 \theta + 2\lambda_z^2 (\cos \theta - |\zeta|)^2 - \frac{\lambda^2 \mathcal{J} (1 - \zeta^2)^2 \sin^4 \theta}{2v^2} - \frac{2\lambda_z^2 \mathcal{J} (\cos \theta - |\zeta|)^4}{v_z^2} \right. \\
& - \frac{\frac{1}{2} \lambda^2 (1 - \zeta^2)^2 \sin^4 \theta + 4\lambda \lambda_z (1 - \zeta^2) \sin^2 \theta (\cos \theta - |\zeta|)^2}{v v_z \left[\frac{(1 - |\zeta| \cos \theta)^2}{v^2} + \frac{(\cos \theta - |\zeta|)^2}{v_z^2} \right]} + 2\zeta^2 (\cos \theta - |\zeta|)^2 \left[2\lambda^2 + \lambda_z^2 - \frac{\lambda^2 (1 - \zeta^2) \sin^2 \theta}{v^2 \left[\frac{(1 - \zeta^2) \sin^2 \theta}{v^2} + \frac{(\cos \theta - |\zeta|)^2}{v_z^2} \right]} \right. \\
& \left. \left. \left. \right\} + \zeta^2 [(2\lambda^2 + \lambda_z^2) - \mathcal{J}'] (\cos \theta - |\zeta|)^2 [\mathcal{I}'^2 + 4\mathcal{I}'(1 - |\zeta| \cos \theta)] \right.
\end{aligned}$$

$$\begin{aligned}
& +3(1 - |\zeta| \cos \theta)^2 - \zeta^2(\cos \theta - |\zeta|)^2 \Big\} - \int_0^\pi d\theta \frac{\sin \theta}{(1 - |\zeta| \cos \theta)^2 [(I' + 1 - |\zeta| \cos \theta)^2 - \zeta^2(\cos \theta - |\zeta|)^2]^2} \\
& \times \frac{\eta_\zeta(1 - \zeta^2)}{16\pi^2 v^2 v_z} \left\{ 2\mathcal{J}' \{ I'^2(1 - \zeta^2) [(\cos \theta - |\zeta|)^2 + \sin^2 \theta] + (1 - \zeta^2)^2 [(\cos \theta - |\zeta|)^2 + \sin^2 \theta]^2 \right. \\
& + 2I'(1 - |\zeta| \cos \theta) [(1 - 2\zeta^2)(\cos \theta - |\zeta|)^2 + (1 - \zeta^2) \sin^2 \theta] \Big\} - \frac{1}{2I'} \{ I'^3 + 2(1 - |\zeta| \cos \theta)^3 + 4I'^2(1 - |\zeta| \cos \theta) \\
& + I' [5(1 - |\zeta| \cos \theta) - \zeta^2(\cos \theta - |\zeta|)^2] \Big\} \left\{ \frac{\lambda^2 \mathcal{J}(1 - \zeta^2)^2 \sin^4 \theta}{2v^2} + \frac{2\lambda_z^2 \mathcal{J}(\cos \theta - |\zeta|)^4}{v_z^2} \right. \\
& + \frac{\frac{1}{2}\lambda^2(1 - \zeta^2)^2 \sin^4 \theta + 4\lambda\lambda_z(1 - \zeta^2) \sin^2 \theta (\cos \theta - |\zeta|)^2}{vv_z \left[\frac{(1 - |\zeta| \cos \theta)^2}{v^2} + \frac{(\cos \theta - |\zeta|)^2}{v_z^2} \right]} + 4 \left\{ \frac{\lambda^2(1 - \zeta^2) \sin^2 \theta}{v^2 \left[\frac{(1 - \zeta^2) \sin^2 \theta}{v^2} + \frac{(\cos \theta - |\zeta|)^2}{v_z^2} \right]} + \frac{\lambda_z^2(\cos \theta - |\zeta|)^2}{v_z^2 \left[\frac{(1 - \zeta^2) \sin^2 \theta}{v^2} + \frac{(\cos \theta - |\zeta|)^2}{v_z^2} \right]} \right\} \\
& \times \zeta^2(\cos \theta - |\zeta|)^2 \Big\} + \zeta^2 \mathcal{J}'(\cos \theta - |\zeta|)^2 [I'^2 + 4I'(1 - |\zeta| \cos \theta) + 3(1 - |\zeta| \cos \theta)^2 - \zeta^2(\cos \theta - |\zeta|)^2] \Big\}, \tag{A13}
\end{aligned}$$

$$\begin{aligned}
\mathcal{D} & \equiv \frac{-\lambda_z^2(1 - \zeta^2)^2 \eta_\zeta}{8\pi^2 v^4 v_z} \int_0^\pi d\theta \frac{\sin^3 \theta}{(1 - |\zeta| \cos \theta)^2 \mathcal{J}^{-1} [(1 - |\zeta| \cos \theta + I)^2 - \zeta^2(\cos \theta - |\zeta|)^2]^2} \\
& \times \left\{ I^2 [(1 - |\zeta| \cos \theta)^2 - \zeta^2(\cos \theta - |\zeta|)^2] + 2I(1 - |\zeta| \cos \theta) [(1 - |\zeta| \cos \theta)^2 - 2\zeta^2(\cos \theta - |\zeta|)^2] \right. \\
& + [(1 - |\zeta| \cos \theta)^2 - \zeta^2(\cos \theta - |\zeta|)^2]^2 \Big\} - \frac{\lambda_z^2(1 - \zeta^2) \eta_\zeta}{32\pi^2 v^2 v_z^3} \int_0^\pi d\theta \frac{\sin \theta (\cos \theta - |\zeta|)^2}{(1 - |\zeta| \cos \theta)^2 \mathcal{J}^{-1} [(1 - |\zeta| \cos \theta + I)^2 - \zeta^2(\cos \theta - |\zeta|)^2]^2} \\
& \times \left\{ I^2 [(1 - |\zeta| \cos \theta)^2 - \zeta^2(\cos \theta - |\zeta|)^2] + 2I'(1 - |\zeta| \cos \theta) [(1 - |\zeta| \cos \theta)^2 - 2\zeta^2(\cos \theta - |\zeta|)^2] \right. \\
& + [(1 - |\zeta| \cos \theta)^2 - \zeta^2(\cos \theta - |\zeta|)^2]^2 \Big\}, \tag{A14}
\end{aligned}$$

$$\begin{aligned}
\mathcal{D}_z & \equiv \frac{(1 - \zeta^2) \eta_\zeta}{8\pi^2 v^2 v_z} \int_0^\pi d\theta \frac{\left\{ \lambda_z^2 \frac{(1 - \zeta^2) \sin^2 \theta}{v^2} - \lambda^2 \left[\frac{(1 - \zeta^2) \sin^2 \theta}{v^2} + \frac{(\cos \theta - |\zeta|)^2}{v_z^2} \right] \right\} \sin \theta}{(1 - |\zeta| \cos \theta)^2 \mathcal{J}^{-1} [(1 - |\zeta| \cos \theta + I)^2 - \zeta^2(\cos \theta - |\zeta|)^2]^2} \\
& \times \left\{ I^2 [(1 - |\zeta| \cos \theta)^2 - \zeta^2(\cos \theta - |\zeta|)^2] + 2I(1 - |\zeta| \cos \theta) [(1 - |\zeta| \cos \theta)^2 - 2\zeta^2(\cos \theta - |\zeta|)^2] + [(1 - |\zeta| \cos \theta)^2 \right. \\
& - \zeta^2(\cos \theta - |\zeta|)^2]^2 \Big\} + \frac{(1 - \zeta^2) \eta_\zeta}{32\pi^2 v^2 v_z} \int_0^\pi d\theta \frac{\sin \theta \left(\lambda_z^2 \frac{(\cos \theta - |\zeta|)^2}{v_z^2} - 2\lambda^2 \frac{(1 - \zeta^2) \sin^2 \theta}{v^2} \right)}{(1 - |\zeta| \cos \theta)^2 \mathcal{J}^{-1} [(1 - |\zeta| \cos \theta + I)^2 - \zeta^2(\cos \theta - |\zeta|)^2]^2} \\
& \times \left\{ I^2 [(1 - |\zeta| \cos \theta)^2 - \zeta^2(\cos \theta - |\zeta|)^2] + 2I'(1 - |\zeta| \cos \theta) [(1 - |\zeta| \cos \theta)^2 - 2\zeta^2(\cos \theta - |\zeta|)^2] \right. \\
& + [(1 - |\zeta| \cos \theta)^2 - \zeta^2(\cos \theta - |\zeta|)^2]^2 \Big\}, \tag{A15}
\end{aligned}$$

$$\begin{aligned}
\mathcal{F}_T^{xx} & = \frac{\eta_\zeta(1 - \zeta^2)}{8\pi^2 v^2 v_z} \int_0^\pi d\theta \frac{\mathcal{J}^2 \sin \theta (1 - |\zeta| \cos \theta)}{I^3} \left[\left(\frac{7}{4} V_T^{xx} + \frac{(V_T^{xy})^2}{V_T^{xx}} + 8 \frac{(V_T^{xz})^2}{V_T^{xx}} + \frac{5}{2} V_T^{xy} \right) \frac{(1 - \zeta^2)^2 \sin^4 \theta}{4v^4} \right. \\
& + \left. \frac{[7(V_T^{xx})^2 + 4(V_T^{xy})^2](-|\zeta| + \cos \theta)^4}{2V_T^{xx} v_z^4} + \left(\frac{7}{2} V_T^{xx} + 2 \frac{(V_T^{xy})^2}{V_T^{xx}} + \frac{5}{2} V_T^{xz} + 2 \frac{V_T^{xy} V_T^{xz}}{V_T^{xx}} \right) \frac{(-|\zeta| + \cos \theta)^2 (1 - \zeta^2) \sin^2 \theta}{v^2 v_z^2} \right], \tag{A16}
\end{aligned}$$

$$\begin{aligned}
\mathcal{F}_T^{zz} & = \frac{\eta_\zeta(1 - \zeta^2)}{8\pi^2 v^2 v_z} \int_0^\pi d\theta \frac{\mathcal{J}^2 \sin \theta (1 - |\zeta| \cos \theta)}{I^3} \left\{ + \frac{[14(V_T^{zz})^2 + 4(V_T^{xz})^2](1 - \zeta^2)^2 \sin^4 \theta}{4V_T^{zz} v^4} + \frac{4(V_T^{xz})^2(-|\zeta| + \cos \theta)^4}{V_T^{zz} v_z^4} \right. \\
& + \left. \frac{[5(V_T^{zz})^2 + 4(V_T^{xz})^2](-|\zeta| + \cos \theta)^2 (1 - \zeta^2) \sin^2 \theta}{V_T^{zz} v^2 v_z^2} \right\}, \tag{A17}
\end{aligned}$$

$$\begin{aligned}
\mathcal{F}_T^{xy} & = \frac{\eta_\zeta(1 - \zeta^2)}{8\pi^2 v^2 v_z} \int_0^\pi d\theta \frac{\mathcal{J}^2 \sin \theta (1 - |\zeta| \cos \theta)}{I^3} \left[\left(\frac{3(V_T^{xx})^2}{2V_T^{xy}} + V_T^{xy} + \frac{V_T^{xx} V_T^{zz}}{2V_T^{xy}} + 8 \frac{(V_T^{xz})^2}{V_T^{xy}} + 3V_T^{xx} \right) \frac{(1 - \zeta^2)^2 \sin^4 \theta}{4v^4} \right. \\
& + \left. \frac{6V_T^{xx}(-|\zeta| + \cos \theta)^4}{v_z^4} + \left(6V_T^{xx} + 2V_T^{zz} + \frac{3V_T^{xx} V_T^{xx}}{V_T^{xy}} \right) \frac{(-|\zeta| + \cos \theta)^2 (1 - \zeta^2) \sin^2 \theta}{v^2 v_z^2} \right], \tag{A18}
\end{aligned}$$

$$\begin{aligned}
\mathcal{F}_T^{xz} & = \frac{\eta_\zeta(1 - \zeta^2)}{8\pi^2 v^2 v_z} \int_0^\pi d\theta \frac{\mathcal{J}^2 \sin \theta (1 - |\zeta| \cos \theta)}{I^3} \left[(2V_T^{xy} + 3V_T^{xx} + 16V_T^{zz}) \frac{(1 - \zeta^2)^2 \sin^4 \theta}{4v^4} \right. \\
& + \left. \frac{(3V_T^{xx} + 2V_T^{xy})(-|\zeta| + \cos \theta)^4}{v_z^4} + (3V_T^{xx} + 2V_T^{zz} + 2V_T^{xy} + \frac{2V_T^{xy} V_T^{zz}}{V_T^{xz}} + \frac{2V_T^{xx} V_T^{zz}}{V_T^{xz}}) \frac{(-|\zeta| + \cos \theta)^2 (1 - \zeta^2) \sin^2 \theta}{v^2 v_z^2} \right], \tag{A19}
\end{aligned}$$

$$\begin{aligned}
\mathcal{F}_L^{xx} & = \frac{\eta_\zeta(1 - \zeta^2)}{8\pi^2 v^2 v_z} \int_0^\pi d\theta \frac{\mathcal{J}^2 \sin \theta (1 - |\zeta| \cos \theta)}{I^3} \left[\left(\frac{7}{4} V_L^{xx} + \frac{(V_L^{xy})^2}{V_L^{xx}} + \frac{5}{2} V_L^{xy} \right) \frac{(1 - \zeta^2)^2 \sin^4 \theta}{4v^4} + \frac{2(V_L^{xz})^2(-|\zeta| + \cos \theta)^4}{V_L^{xx} v_z^4} \right.
\end{aligned}$$

$$+ \left(\frac{5}{2} V_L^{xz} + 2 \frac{V_L^{xy} V_L^{xz}}{V_L^{xx}} \right) \frac{(-|\zeta| + \cos \theta)^2 (1 - \zeta^2) \sin^2 \theta}{v^2 v_z^2} \Big], \quad (\text{A20})$$

$$\mathcal{F}_L^{zz} = \frac{\eta_\zeta (1 - \zeta^2)}{8\pi^2 v^2 v_z} \int_0^\pi d\theta \frac{\mathcal{J}^2 \sin \theta (1 - |\zeta| \cos \theta)}{\mathcal{I}^3} \left[\frac{4(V_L^{xz})^2 (1 - \zeta^2)^2 \sin^4 \theta}{4V_L^{zz} v^4} + \frac{7V_L^{zz} (-|\zeta| + \cos \theta)^4}{2v_z^4} \right. \\ \left. + \frac{5V_L^{xz} (-|\zeta| + \cos \theta)^2 (1 - \zeta^2) \sin^2 \theta}{v^2 v_z^2} \right], \quad (\text{A21})$$

$$\mathcal{F}_L^{xy} = \frac{\eta_\zeta (1 - \zeta^2)}{8\pi^2 v^2 v_z} \int_0^\pi d\theta \frac{\mathcal{J}^2 \sin \theta (1 - |\zeta| \cos \theta)}{\mathcal{I}^3} \left[\left(\frac{9V_L^{xx}}{4V_T^{xy}} + V_L^{xy} + 3V_L^{xx} \right) \frac{(1 - \zeta^2)^2 \sin^4 \theta}{4v^4} + \frac{2(V_T^{xz})^2 (-|\zeta| + \cos \theta)^4}{V_L^{xy} v_z^4} \right. \\ \left. + \left(2V_L^{xz} + \frac{3V_L^{xx} V_L^{xz}}{V_L^{xy}} \right) \frac{(-|\zeta| + \cos \theta)^2 (1 - \zeta^2) \sin^2 \theta}{v^2 v_z^2} \right], \quad (\text{A22})$$

$$\mathcal{F}_L^{xz} = \frac{\eta_\zeta (1 - \zeta^2)}{8\pi^2 v^2 v_z} \int_0^\pi d\theta \frac{\mathcal{J}^2 \sin \theta (1 - |\zeta| \cos \theta)}{\mathcal{I}^3} \left[\frac{(4V_L^{xx} + 2V_L^{xy})(1 - \zeta^2)^2 \sin^4 \theta}{4v^4} + 3V_L^{zz} \frac{(-|\zeta| + \cos \theta)^4}{v_z^4} \right. \\ \left. + \left(2V_L^{xz} + \frac{11V_L^{xx} V_L^{zz}}{4V_L^{xz}} + \frac{3V_L^{xy} V_L^{zz}}{2V_L^{xz}} \right) \frac{(-|\zeta| + \cos \theta)^2 (1 - \zeta^2) \sin^2 \theta}{v^2 v_z^2} \right], \quad (\text{A23})$$

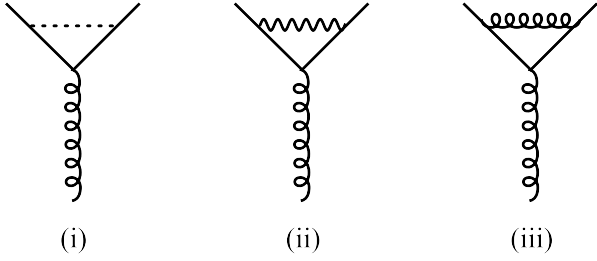


FIG. 22: One-loop corrections to the strength of source term Δ_i due to (a) the electron-phonon interaction, (b) the Coulomb interaction, and the source-term itself, respectively.

with \mathcal{I} , \mathcal{I}' , \mathcal{J} , and \mathcal{J}' being defined as

$$\mathcal{I} \equiv \sqrt{C_T^2 \frac{(1 - \zeta^2) \sin^2 \theta}{v^2} + C_{T_z}^2 \frac{(\cos \theta - |\zeta|)^2}{v_z^2}}, \quad (\text{A24})$$

$$\mathcal{I}' \equiv \sqrt{C_L^2 \frac{(1 - \zeta^2) \sin^2 \theta}{v^2} + C_{L_z}^2 \frac{(\cos \theta - |\zeta|)^2}{v_z^2}}, \quad (\text{A25})$$

$$\mathcal{J} \equiv \left[\frac{(\cos \theta - |\zeta|)^2 (1 - \zeta^2) \sin^2 \theta}{v_z^2 v^2} \right]^{-1}, \quad (\text{A26})$$

$$\mathcal{J}' \equiv \frac{\lambda^2 \frac{(1 - \zeta^2) \sin^2 \theta}{v^2} + \lambda_z^2 \frac{(\cos \theta - |\zeta|)^2}{v_z^2}}{\frac{(1 - \zeta^2) \sin^2 \theta}{v^2} + \frac{(\cos \theta - |\zeta|)^2}{v_z^2}}. \quad (\text{A27})$$

Appendix B: Energy-dependent evolutions of source terms

After completing the calculations for the one-loop corrections to the strengths of the source terms $\Delta_i^{\text{PH/PP}}$

shown in Fig. 22, we then can derive the RG equations with the help of RG rescalings (16)-(21). The concrete RG equations are listed as follows,

$$\frac{d\Delta_0^{\text{PH}}}{dl} = (1 - 2\eta_\psi) \Delta_0^{\text{PH}}, \quad (\text{B1})$$

$$\frac{d\Delta_1^{\text{PH}}}{dl} = [1 - 2\eta_\psi + (\mathcal{R}_1^+ - \mathcal{R}_1^-)(-g^2 - \lambda_z^2)] \Delta_1^{\text{PH}}, \quad (\text{B2})$$

$$\frac{d\Delta_2^{\text{PH}}}{dl} = [1 - 2\eta_\psi + (\mathcal{R}_2^+ - \mathcal{R}_2^-)(-g^2 - \lambda_z^2)] \Delta_2^{\text{PH}}, \quad (\text{B3})$$

$$\frac{d\Delta_3^{\text{PH}}}{dl} = [1 - 2\eta_\psi + (\mathcal{R}_3^+ - \mathcal{R}_3^-)(\lambda_z^2 - g^2 - 2\lambda^2)] \Delta_3^{\text{PH}} \quad (\text{B4})$$

for the particle-hole channel, and

$$\frac{d\Delta_0^{\text{PP}}}{dl} = [1 - 2\eta_\psi + (\mathcal{T}_0^+ - \mathcal{T}_0^-)(-g^2 - \lambda_z^2)] \Delta_0^{\text{PP}}, \quad (\text{B5})$$

$$\frac{d\Delta_1^{\text{PP}}}{dl} = [1 - 2\eta_\psi + (\mathcal{T}_1^+ - \mathcal{T}_1^-)(\lambda_z^2 - g^2 - 2\lambda^2)] \Delta_1^{\text{PP}} \quad (\text{B6})$$

$$\frac{d\Delta_2^{\text{PP}}}{dl} = [1 - 2\eta_\psi + (\mathcal{T}_2^+ - \mathcal{T}_2^-)(-g^2 - \lambda_z^2)] \Delta_2^{\text{PP}}, \quad (\text{B7})$$

$$\frac{d\Delta_{30}^{\text{PP}}}{dl} = [1 - 2\eta_\psi + (\mathcal{T}_0^+ - \mathcal{T}_0^-)(-g^2 - \lambda_z^2)] \Delta_{30}^{\text{PP}}, \quad (\text{B8})$$

$$\frac{d\Delta_{31}^{\text{PP}}}{dl} = [1 - 2\eta_\psi + (\mathcal{T}_1^+ - \mathcal{T}_1^-)(\lambda_z^2 - g^2 - 2\lambda^2)] \Delta_{31}^{\text{PP}} \quad (\text{B9})$$

$$\frac{d\Delta_{33}^{\text{PP}}}{dl} = [1 - 2\eta_\psi + (\mathcal{T}_2^+ - \mathcal{T}_2^-)(-g^2 - \lambda_z^2)] \Delta_{33}^{\text{PP}}, \quad (\text{B10})$$

for the particle-particle channel, where all the related coefficients are designated as

$$\mathcal{R}_1^+ = \int_0^\pi \frac{(1 - \zeta \cos \theta) |\zeta^2 - 1| \sin \theta (\cos^2 \theta - \zeta^2 \cos^2 \theta + \zeta^2 - 4\zeta \sqrt{1 - \zeta^2} \cos \theta + 1)}{16\pi^2 (\zeta^2 - 1)^2 (1 - 2\zeta \sqrt{1 - \zeta^2} \cos \theta)^{\frac{3}{2}}} d\theta, \quad (\text{B11})$$

$$\mathcal{R}_1^- = \int_0^\pi \frac{(1 + \zeta \cos \theta) |\zeta^2 - 1| \sin \theta (\cos^2 \theta - \zeta^2 \cos^2 \theta + \zeta^2 + 4\zeta \sqrt{1 - \zeta^2} \cos \theta + 1)}{16\pi^2 (\zeta^2 - 1)^2 (1 + 2\zeta \sqrt{1 - \zeta^2} \cos \theta)^{\frac{3}{2}}} d\theta, \quad (\text{B12})$$

$$\mathcal{R}_2^+ = \int_0^\pi \frac{(1 - \zeta \cos \theta) |\zeta^2 - 1| \sin \theta (\cos^2 \theta - \zeta^2 \cos^2 \theta + \zeta^2 - 4\zeta \sqrt{1 - \zeta^2} \cos \theta + 1)}{16\pi^2 (\zeta^2 - 1)^2 (1 - 2\zeta \sqrt{1 - \zeta^2} \cos \theta)^{\frac{3}{2}}} d\theta, \quad (\text{B13})$$

$$\mathcal{R}_2^- = \int_0^\pi \frac{(1 + \zeta \cos \theta) |\zeta^2 - 1| \sin \theta (\cos^2 \theta - \zeta^2 \cos^2 \theta + \zeta^2 + 4\zeta \sqrt{1 - \zeta^2} \cos \theta + 1)}{16\pi^2 (\zeta^2 - 1)^2 (1 + 2\zeta \sqrt{1 - \zeta^2} \cos \theta)^{\frac{3}{2}}} d\theta, \quad (\text{B14})$$

$$\mathcal{R}_3^+ = \int_0^\pi \frac{(1 - \zeta \cos \theta) |\zeta^2 - 1| \sin \theta (\cos^2 \theta - 1)}{16\pi^2 (\zeta^2 - 1) (1 - 2\zeta \sqrt{1 - \zeta^2} \cos \theta)^{\frac{3}{2}}} d\theta, \quad (\text{B15})$$

$$\mathcal{R}_3^- = \int_0^\pi \frac{(1 + \zeta \cos \theta) |\zeta^2 - 1| \sin \theta (\cos^2 \theta - 1)}{16\pi^2 (\zeta^2 - 1) (1 + 2\zeta \sqrt{1 - \zeta^2} \cos \theta)^{\frac{3}{2}}} d\theta, \quad (\text{B16})$$

and

$$\mathcal{T}_0^+ = \int_0^\pi \frac{\sin^3 \theta (1 - \zeta \cos \theta)}{16\pi^2 \zeta (1 - \zeta)^2 \left(\frac{\cos \theta}{\sqrt{1 - \zeta^2}} - \frac{\zeta}{1 - \zeta^2} \right) \left[\sin^2 \theta - (\zeta^2 - 1) \left(\cos^2 \theta - \frac{2\zeta}{\sqrt{1 - \zeta^2}} + \frac{\zeta^2}{1 - \zeta^2} \right) \right]} d\theta, \quad (\text{B17})$$

$$\mathcal{T}_0^- = \int_0^\pi \frac{\sin^3 \theta (1 + \zeta \cos \theta)}{16\pi^2 \zeta (1 - \zeta)^2 \left(\frac{\cos \theta}{\sqrt{1 - \zeta^2}} - \frac{\zeta}{1 - \zeta^2} \right) \left[\sin^2 \theta - (\zeta^2 - 1) \left(\cos^2 \theta + \frac{2\zeta}{\sqrt{1 - \zeta^2}} + \frac{\zeta^2}{1 - \zeta^2} \right) \right]} d\theta, \quad (\text{B18})$$

$$\mathcal{T}_1^+ = \int_0^\pi \frac{\sin \theta (1 - \zeta \cos \theta) \left(\cos^2 \theta - \frac{2\zeta}{\sqrt{1 - \zeta^2}} \cos \theta + \frac{\zeta^2}{1 - \zeta^2} \right)}{16\pi^2 \zeta (1 - \zeta^2)^2 \left(\frac{\cos \theta}{\sqrt{1 - \zeta^2}} - \frac{\zeta}{1 - \zeta^2} \right) \left[\sin^2 \theta - (\zeta^2 - 1) \left(\cos^2 \theta - \frac{2\zeta}{\sqrt{1 - \zeta^2}} + \frac{\zeta^2}{1 - \zeta^2} \right) \right]} d\theta, \quad (\text{B19})$$

$$\mathcal{T}_1^- = \int_0^\pi \frac{\sin \theta (1 + \zeta \cos \theta) \left(\cos^2 \theta + \frac{2\zeta}{\sqrt{1 - \zeta^2}} \cos \theta + \frac{\zeta^2}{1 - \zeta^2} \right)}{16\pi^2 \zeta (1 - \zeta^2)^2 \left(\frac{\cos \theta}{\sqrt{1 - \zeta^2}} - \frac{\zeta}{1 - \zeta^2} \right) \left[\sin^2 \theta - (\zeta^2 - 1) \left(\cos^2 \theta + \frac{2\zeta}{\sqrt{1 - \zeta^2}} + \frac{\zeta^2}{1 - \zeta^2} \right) \right]} d\theta, \quad (\text{B20})$$

$$\mathcal{T}_2^+ = \int_0^\pi \frac{-\sin^3 \theta (1 - \zeta \cos \theta)}{16\pi^2 \zeta (1 - \zeta^2)^2 \left(\frac{\cos \theta}{\sqrt{1 - \zeta^2}} - \frac{\zeta}{1 - \zeta^2} \right) \left[\sin^2 \theta - (\zeta^2 - 1) \left(\cos^2 \theta - \frac{2\zeta}{\sqrt{1 - \zeta^2}} + \frac{\zeta^2}{1 - \zeta^2} \right) \right]} d\theta, \quad (\text{B21})$$

$$\mathcal{T}_2^- = \int_0^\pi \frac{-\sin^3 \theta (1 + \zeta \cos \theta)}{16\pi^2 \zeta (1 - \zeta^2)^2 \left(\frac{\cos \theta}{\sqrt{1 - \zeta^2}} - \frac{\zeta}{1 - \zeta^2} \right) \left[\sin^2 \theta - (\zeta^2 - 1) \left(\cos^2 \theta + \frac{2\zeta}{\sqrt{1 - \zeta^2}} + \frac{\zeta^2}{1 - \zeta^2} \right) \right]} d\theta. \quad (\text{B22})$$

-
- [1] K. S. Novoselov, A. K. Geim, S. V. Morozov, D. Jiang, M. I. Katsnelson, I. V. Grigorieva, S. V. Dubonos, and A. A. Firsov, *Nature* **438**, 197 (2005).
- [2] A. H. Castro Neto, F. Guinea, N. M. R. Peres, K. S. Novoselov, and A. K. Geim, *Rev. Mod. Phys.* **81**, 109 (2009).
- [3] J. E. Moore, *Nature* **464**, 194 (2010).
- [4] M. Z. Hasan and C. L. Kane, *Rev. Mod. Phys.* **82**, 3045 (2010).
- [5] X. L. Qi and S. C. Zhang, *Rev. Mod. Phys.* **83**, 1057 (2011).
- [6] P. Dietl, F. Piéchon, and G. Montambaux, *Phys. Rev. Lett.* **100**, 236405 (2008); G. Montambaux, F. Piéchon, J. -N. Fuchs, and M. O. Goerbig, *Phys. Rev. B* **80**, 153412 (2009); P. Delplace and G. Montambaux, *Phys. Rev. B* **82**, 035438 (2010); L. -K. Lim, J. -N. Fuchs, and Gilles Montambaux, *Phys. Rev. Lett.* **108**, 175303 (2012).
- [7] L. Savary, J. Ruhman, J. W. F. Venderbos, L. Fu, and P. A. Lee, *Phys. Rev. B* **96**, 214514 (2017).
- [8] L. Savary, E. -G. Moon and L. Balents, *Phys. Rev. X* **4**, 041027 (2014); H. Oh, S. Lee, Y. -B. Kim, and E. -G. Moon, *Phys. Rev. Lett.* **122**, 167201 (2019).
- [9] J. -A. Steinberg, S. -M. Young, S. Zaheer, C. -L. Kane, E. -J. Mele, and A. -M. Rappe, *Phys. Rev. Lett.* **112**, 036403 (2014).
- [10] Z. J. Wang, Y. Sun, X. Q. Chen, C. Franchini, G. Xu, H.-M. Weng, X. Dai, and Z. Fang, *Phys. Rev. B* **85**, 195320 (2012).
- [11] S. M. Young, S. Zaheer, J. C. Y. Teo, C. L. Kane, E. J. Mele and A. M. Rappe, *Phys. Rev. Lett.* **108**, 140405 (2012).
- [12] Z. K. Liu, J. Jiang, B. Zhou, Z. J. Wang, Y. Zhang, H. M. Weng, D. Prabhakaran, S. K. Mo, H. Peng, P. Dudin, T. Kim, M. Hoesch, Z. Fang, X. Dai, Z. X. Shen, D. L. Feng, Z. Hussain, and Y. L. Chen, *Nat. Mater.* **13**, 677 (2014).
- [13] Z. K. Liu, B. Zhou, Y. Zhang, Z. J. Wang, H. M. Weng, D. Prabhakaran, S. K. Mo, Z. X. Shen, Z. Fang, X. Dai, Z. Hussain, and Y. L. Chen, *Science* **343**, 864 (2014).

- [14] O. Vafek and A. Vishwanath, *Annu. Rev. Condens. Matter Phys.* **5**, 83 (2014).
- [15] T. O. Wehling, A. M. Black-Schaffer, and A. V. Balatsky, *Adv. Phys.* **63**, 1 (2014).
- [16] J. Xiong, S. K. Kushwaha, T. Liang, J. W. Krizan, M. Hirschberger, W. Wang, R. J. Cava and N. P. Ong, *Science* **350**, 413 (2015).
- [17] R. Roy, *Phys. Rev. B* **79**, 195322 (2009).
- [18] B. Roy, S. Das Sarma, *Phys. Rev. B* **94**, 115137 (2016); B. Roy, Y. Alavirad, and J. D. Sau, *Phys. Rev. Lett.* **94**, 227002 (2017); B. Roy, R. -J. Slager, and V. Juricic, *Phys. Rev. X* **8**, 031076 (2018); B. Roy, V. Juricic, and S. Das Sarma, *Sci. Rep.* **6**, 32446 (2016).
- [19] H. -H. Lai, B. Roy, and P. Goswami, arXiv: 1409.8675 (2014); P. Goswami, B. Roy, and S. Das Sarma, *Phys. Rev. B* **95**, 085120 (2017); A. L. Szabo, R. Moessner, and B. Roy, *Phys. Rev. B* **103**, 165139 (2021); B. Roy, S. A. Akbar Ghorashi, M. S. Foster, and A. H. Nevidomskyy, *Phys. Rev. B* **99**, 054505 (2019).
- [20] M. M. Korshunov, D. V. Efremov, A. A. Golubov and O. V. Dolgov, *Phys. Rev. B* **90**, 134517 (2014).
- [21] H. H. Hung, A. Barr, E. Prodan and G. A. Fiete, *Phys. Rev. B* **94**, 235132 (2016).
- [22] R. Nandkishore, J. Maciejko, D. A. Huse, and S. L. Sondhi, *Phys. Rev. B* **87**, 174511 (2013).
- [23] I. D. Potirniche, J. Maciejko, R. Nandkishore, and S. L. Sondhi, *Phys. Rev. B* **90**, 094516 (2014).
- [24] R. M. Nandkishore and S. A. Parameswaran, *Phys. Rev. B* **95**, 205106 (2017).
- [25] A. A. Soluyanov, D. Gresch, Z. J. Wang, Q. S. Wu, M. Troyer, X. Dai, and B. A. Bernevig, *Nature (London)* **527**, 495 (2015).
- [26] M. Trescher, B. Sbierski, P. W. Brouwer, and E. J. Bergholtz, *Phys. Rev. B* **91**, 115135 (2015).
- [27] S. A. Jafari, *Phys. Rev. B* **100**, 045144 (2019).
- [28] Y. Mao, W. L. Wang, D. Wei, E. Kaxiras, and J. G. Soderoski, *ACS Nano* **5**, 1395 (2011).
- [29] Y. -W. Lee and Y. -L. Lee, *Phys. Rev. B* **97**, 035141 (2018).
- [30] Y. -L. Lee and Y. -W. Lee, *Phys. Rev. B* **100**, 075156 (2019).
- [31] H. J. Noh, J. Jeong, E. J. Cho, K. Kim, B. I. Min, and B. G. Park, *Phys. Rev. Lett.* **119**, 016401 (2017).
- [32] F. C. Fei, X. Y. Bo, R. Wang, B. Wu, J. Jiang, D. Z. Fu, M. Gao, H. Zheng, Y. L. Chen, X. F. Wang, H. J. Bu, F. Q. Song, X. G. Wang, B. G. Wang, and G. H. Wang, *Phys. Rev. B* **96**, 041201(R) (2017).
- [33] N. M. R. Peres, *Rev. Mod. Phys.* **82**, 2673 (2010).
- [34] S. Katayama, A. Kobayashi, and Y. Suzumura, *J. Phys. Soc. Jpn.* **75**, 054705 (2006).
- [35] A. Kobayashi, S. Katayama, Y. Suzumura, and H. Fukuyama, *J. Phys. Soc. Jpn.* **76**, 034711 (2007).
- [36] M. O. Goerbig, J. -N. Fuchs, G. Montambaux, and F. Piéchon, *Phys. Rev. B* **78**, 045415 (2008).
- [37] Y. Xu, F. Zhang, and C. Zhang, *Phys. Rev. Lett.* **115**, 265304 (2015).
- [38] Y. Xu and L. -M. Duan, *Phys. Rev. A* **94**, 053619 (2016).
- [39] S. A. Jafari, *Eur. Phys. J. B* **68**, 537 (2009); Z. Jalali-Mola and S. A. Jafari, *Phys. Rev. B* **100**, 075113 (2019).
- [40] M. Z. Yan, H. Q. Huang, K. N. Zhang, E. Wang, W. Yao, K. Deng, G. L. Wan, H. Y. Zhang, M. Arita, H. T. Yang, Z. Sun, H. Yao, Y. Wu, S. S. Fan, W. H. Duan, and S. Y. Zhou, *Nat. Commun* **8**, 257 (2017).
- [41] F. Detassis, L. Fritz, and S. Grubinskas, *Phys. Rev. B* **96**, 195157 (2017).
- [42] J. Q. Li, D. X. Zheng, and J. Wang, *Eur. Phys. J. B* **92**, 274 (2019).
- [43] C. Shekhar, A. K. Nayak, Y. Sun, M. Schmidt, M. Nicklas, I. Leermakers, U. Zeitler, Y. Skourski, J. Wosnitza, Z. Liu, Y. Chen, W. Schnelle, H. Borrmann, Y. Grin, C. Felser, and B. Yan, *Nature Physics* **11**, 3372 (2015).
- [44] S. A. Parameswaran, T. Grover, D. A. Abanin, D. A. Pesin, and A. Vishwanath, *Phys. Rev. X* **4**, 031035 (2014).
- [45] A. C. Potter, I. Kimchi, and A. Vishwanath, *Nature Communications* **5**, 5161 (2014).
- [46] Y. Baum, E. Berg, S. A. Parameswaran, and A. Stern, *Phys. Rev. X* **5**, 041046 (2015).
- [47] F. Arnold, C. Shekhar, S. -C. Wu, Y. Sun, R. D. dos Reis, N. Kumar, M. Naumann, M. O. Ajeesh, M. Schmidt, A. G. Grushin, J. H. Bardarson, M. Baenitz, D. Sokolov, H. Borrmann, M. Nicklas, C. Felser, E. Hassinger, and B. Yan, *Nature Communications* **7**, 11615 (2016).
- [48] C. -L. Zhang, S. -Y. Xu, I. Belopolski, Z. Yuan, Z. Lin, B. Tong, G. Bian, N. Alidoust, C. -C. Lee, S. -M. Huang, T. R. Chang, G. Chang, C. -H. Hsu, H. -T. Jeng, M. Neupane, D. S. Sanchez, H. Zheng, J. Wang, H. Lin, C. Zhang, H. -Z. Lu, S. -Q. Shen, T. Neupert, M. Zahid Hasan, and S. Jia, *Nature Communications* **7**, 10735 (2016).
- [49] T. S. Sikkenk and L. Fritz, *Phys. Rev. B* **100**, 085121 (2019).
- [50] Z. Jalali-Mola and S. A. Jafari, *Phys. Rev. B* **98**, 195415 (2018).
- [51] Z. -K. Yang, J. -R. Wang, and G. -Z. Liu, *Phys. Rev. B* **98**, 195123 (2018).
- [52] I. Proskurin, M. Ogata, and Y. Suzumura, *Phys. Rev. B* **91**, 195413 (2015).
- [53] T. E. O'Brien, M. Diez, and C. W. J. Beenakker, *Phys. Rev. Lett.* **116**, 236401 (2016); Z. M. Yu, Y. Yao, and S. A. Yang, *Phys. Rev. Lett.* **117**, 077202 (2016); M. Udagawa and E. J. Bergholtz, *Phys. Rev. Lett.* **117**, 086401 (2016); S. Tchoumakov, M. Civelli, and M. O. Goerbig, *Phys. Rev. Lett.* **117**, 086402 (2016).
- [54] A. A. Zyuzin and R. P. Tiwari, *JETP Lett.* **103**, 717 (2016); J. F. Steiner, A. V. Andreev, and D. A. Pesin, *Phys. Rev. Lett.* **119**, 036601 (2017).
- [55] Y. Ferreira, A. A. Zyuzin, and J. H. Bardarson, *Phys. Rev. B* **96**, 115202 (2017); S. Saha and S. Tewari, *Eur. Phys. J. B* **91**, 4 (2018).
- [56] M. Alidoust and K. Halterman, *Phys. Rev. B* **101**, 035120 (2020).
- [57] V. Kozii, Z. Bi, and J. Ruhman, *Phys. Rev. X* **9**, 031046 (2019).
- [58] K. G. Wilson, *Rev. Mod. Phys.* **47** 773 (1975).
- [59] J. Polchinski, arXiv: hep-th/9210046 (1992).
- [60] R. Shankar, *Rev. Mod. Phys.* **66**, 129 (1994).
- [61] D. E. Khmel'nitskii and V. L. Shneerson, *Sov. Phys. Solid State* **13**, 687 (1971).
- [62] B. A. Strukov and A. P. Levanyuk, *Ferroelectric Phenomena in Crystals: Physical Foundations* (Springer Science, New York, 2012)
- [63] G. -Y. Cho and E. -G. Moon, *Sci. Rep.* **6**, 19198 (2016).

- [64] Ye. Huh, E. -G. Moon, and Y. -B. Kim, Phys. Rev. B **93**, 035138 (2016).
- [65] I. Mandal and H. Freire, Phys. Rev. B **103**, 195116 (2022).
- [66] Y. Huh, S. Sachdev, Phys. Rev. B **78**, 064512 (2008); E. -A. Kim, M. J. Lawler, P. Oretto, S. Sachdev, E. Fradkin, and S. A. Kivelson, Phys. Rev. B **77**, 184514 (2008).
- [67] J. -H She, J. Zaanen, A. R. Bishop, and A. V. Balatsky, Phys. Rev. B **82**, 165128 (2010).
- [68] J. Wang, G. -Z. Liu, and H. Kleinert, Phys. Rev. B **83**, 214503 (2011).
- [69] Y. M. Dong, Y. H. Zhai, D. X. Zheng, and J. Wang, Phys. Rev. B **102**, 134204 (2020).
- [70] S. Maiti and A.V. Chubukov, Phys. Rev. B **82**, 214515 (2010).
- [71] C. J. Halboth and W. Metzner, Phys. Rev. Lett. **85**, 5162 (2000).
- [72] C. J. Halboth and W. Metzner, Phys. Rev. B **61**, 7364 (2000).
- [73] R. Nandkishore, L. S. Levitov, and A. V. Chubukov, Nat. Phys. **8**, 158 (2012).
- [74] V. Cvetković, R. E. Throckmorton, and O. Vafek, Phys. Rev. B **86**, 075467 (2012).
- [75] J. Wang, Nuclear Physics B **961**, 115230 (2020).
- [76] O. Vafek, Phys. Rev. B **82**, 205106 (2010).
- [77] J. M. Murray and O. Vafek, Phys. Rev. B **89**, 201110(R) (2014).
- [78] Y. H. Zhai and J. Wang, Nucl. Phys. B **966**, 115371 (2021).
- [79] A. L. Szabó and B. Roy, arXiv: 2009.05055 (2020).
- [80] B. Roy and M. S. Foster, Phys. Rev. X **8**, 011049 (2018).
- [81] G. D. Mahan, Many-Particle Physics, 2nd edn. (Plenum, New York, 1982).
- [82] J. Wang and G. -Z. Liu, Phys. Rev. D **85**, 105010 (2012).
- [83] F. Schwabl, Statistical Mechanics (Springer, Berlin, 2006), 2nd ed.
- [84] E. -H. Hwang and B. Y. K. Hu, and S. -D. Sarma, Phys. Rev. Lett. **99**, 226801 (2007).
- [85] J. I. Kapusta and C. Gale, Finite-Temperature Field Theory: Principles and Applications (Cambridge University Press, Cambridge, 2006).